# From giant clumps to clouds - III. The connection between star formation and turbulence in the ISM

(article starts on next page)

# From giant clumps to clouds – III. The connection between star formation and turbulence in the ISM

Timmy Ejdetjärn [ORCID],[1,2]★ Oscar Agertz [ORCID],[2] Göran Östlin,[1] Florent Renaud [ORCID][2] and Alessandro B. Romeo[3]

[1]*Oskar Klein Centre, Department of Astronomy, Stockholm University, SE-10691 Stockholm, Sweden*
[2]*Department of Astronomy and Theoretical Physics, Lund Observatory, Box 43, SE-22100 Lund, Sweden*
[3]*Department of Space, Earth and Environment, Chalmers University of Technology, SE-41296 Gothenburg, Sweden*

## ABSTRACT

Supersonic gas turbulence is a ubiquitous property of the interstellar medium. The level of turbulence, quantified by the gas velocity dispersion ($\sigma_g$), is observed to increase with the star formation rate (SFR) of a galaxy, but it is yet not established whether this trend is driven by stellar feedback or gravitational instabilities. In this work, we carry out hydrodynamical simulations of entire disc galaxies, with different gas fractions, to understand the origins of the SFR–$\sigma_g$ relation. We show that disc galaxies reach the same levels of turbulence regardless of the presence of stellar feedback processes, and argue that this is an outcome of the way disc galaxies regulate their gravitational stability. The simulations match the SFR–$\sigma_g$ relation up to SFRs of the order of tens of $M_\odot \, \mathrm{yr}^{-1}$ and $\sigma_g \sim 50 \, \mathrm{km \, s}^{-1}$ in neutral hydrogen and molecular gas, but fail to reach the very large values ($> 100 \, \mathrm{km \, s}^{-1}$) reported in the literature for rapidly star-forming galaxies. We demonstrate that such high values of $\sigma_g$ can be explained by (1) insufficient beam smearing corrections in observations and (2) stellar feedback being coupled to the ionized gas phase traced by recombination lines. Given that the observed SFR–$\sigma_g$ relation is composed of highly heterogeneous data, with $\sigma_g$ at high SFRs almost exclusively being derived from H $\alpha$ observations of high-redshift galaxies with complex morphologies, we caution against analytical models that attempt to explain the SFR–$\sigma_g$ relation without accounting for these effects.

**Key words:** turbulence – methods: numerical – ISM: evolution – ISM: kinematics and dynamics – galaxies: star formation.

## 1 INTRODUCTION

The interstellar medium (ISM) of disc galaxies is observed to be highly dynamic and complex in nature. A striking property of the ISM is its supersonic turbulence across a wide range of spatial scales, redshifts, and a multitude of gas tracers (see e.g. Elmegreen & Scalo 2004; Mac Low & Klessen 2004; Glazebrook 2013, for reviews). The presence of supersonic turbulence has been found to have a crucial impact on the temperature and density distribution in the galaxy (e.g. McKee & Ostriker 2007), gas mixing (Yang & Krumholz 2012; Armillotta, Krumholz & Fujimoto 2018), and the formation of stars (Mac Low & Klessen 2004; Ballesteros-Paredes et al. 2007; Renaud, Kraljic & Bournaud 2012; Padoan et al. 2014; Federrath 2018).

The dynamics of the ISM in galaxies through a large range of evolutionary stages is well observed with several tracers, corresponding to different distinct gas phases. The level of turbulent gas motions, commonly quantified as the velocity dispersion $\sigma_g$ (measured as the line width of individual emission lines), can vary significantly between phases. In the warm ionized phase of local disc galaxies, it is of the order of $\sigma_g \sim 10$–$40 \, \mathrm{km \, s}^{-1}$ (e.g. Moiseev, Tikhonov & Klypin 2015; Varidel et al. 2016) and it rises to $\gtrsim 100 \, \mathrm{km \, s}^{-1}$ in rapidly star-forming high-redshift galaxies (e.g. Cresci et al. 2009; Epinat et al. 2009; Law et al. 2009; Genzel et al. 2011; Alcorn et al. 2018). In contrast, in local disc galaxies, the velocity dispersion in

atomic hydrogen (Ianjamasimanana et al. 2012; Stilp et al. 2013) and molecular hydrogen (e.g. Caldú-Primo et al. 2013; Nguyen-Luong et al. 2016; Levy et al. 2018; Girard et al. 2021) is commonly observed around $\sigma_g \sim 10 \, \mathrm{km \, s}^{-1}$.

A relation between the star formation rates (SFRs) of galaxies and $\sigma_g$ is observed across several observed scales, redshifts, and gas tracers (e.g. Epinat et al. 2009; Ianjamasimanana et al. 2012; Moiseev et al. 2015; Alcorn et al. 2018; Levy et al. 2018). This implies that the process of star formation is accompanied by the injection of turbulence in the ISM. However, there is no consensus on what drives and maintains the ISM turbulence. A large number of candidates have been argued in literature (see Elmegreen & Scalo 2004; Glazebrook 2013, for a review), with some combination of stellar feedback and gravitational instabilities likely being important (e.g. Dib, Bell & Burkert 2006; Agertz et al. 2009; Lehnert et al. 2009; Krumholz et al. 2018; Orr, Hayward & Hopkins 2019). Stellar feedback intuitively fits the scenario, as supernovae and stellar winds naturally insert large amounts of energy and momentum into the ISM, and has a close connection to star formation. However, gravitational instabilities are also closely connected to the formation of stars and can convert potential energy into turbulent energy, e.g. in the form of clump formation, accretion or radial flows through the disc (e.g. Agertz et al. 2009; Dekel et al. 2009a; Krumholz & Burkert 2010). Cosmological processes, such as accretion and mergers, have also been suggested to directly induce turbulence during interactions (e.g. Förster Schreiber et al. 2006; Dekel, Sari & Ceverino 2009b; Klessen & Hennebelle 2010; Genel, Dekel & Cacciato 2012; Renaud

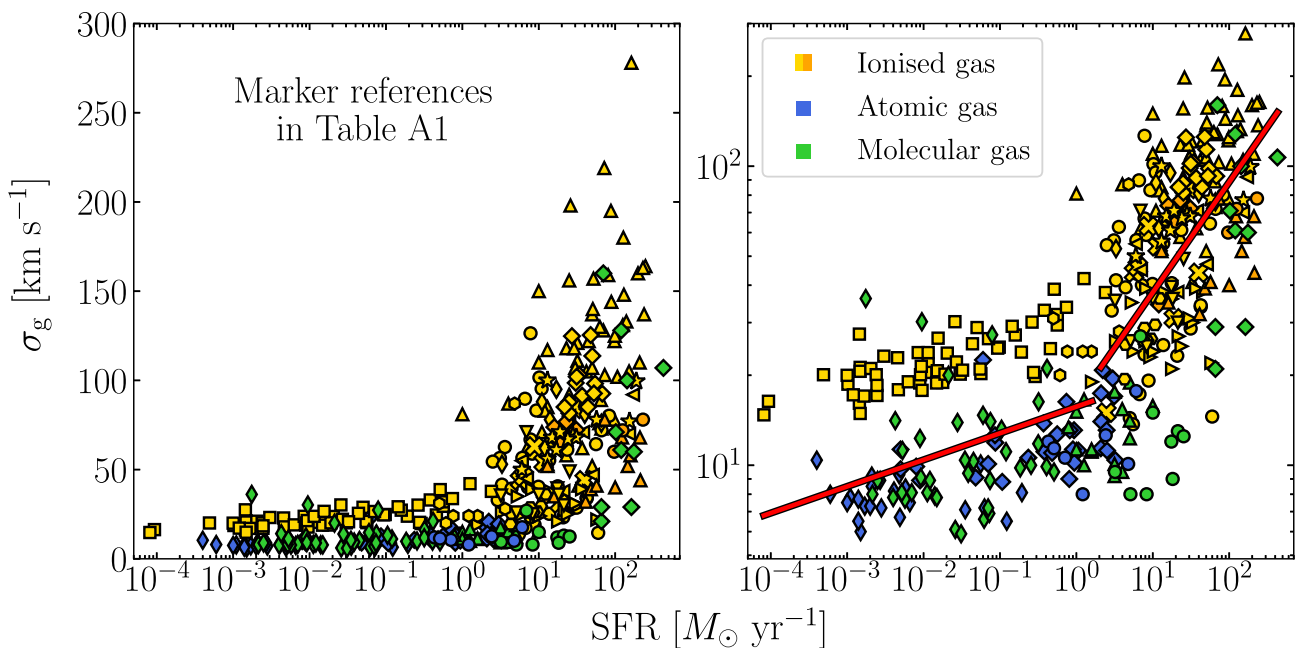★ E-mail: timmy.ejdetjarn@astro.su.se

**Figure 1.** Observational data of the relation between the gas velocity dispersion $\sigma_{\mathrm{g}}$ (a measurement on the level of gas turbulence) and the SFR. The markers represent individual galaxies (sources and additional information shown in Table A1) and are colour-coded by the gas phase of the tracer used to measure $\sigma_{\mathrm{g}}$. Left-hand figure shows the relation as it is commonly evaluated in literature and the right-hand figure shows the relation in log-space in order to highlight the kinematic difference at some threshold SFR $\sim 2\,\mathrm{M}_{\odot}\,\mathrm{yr}^{-1}$; further illustrated by the two fitted (red) lines. The data set is highly heterogeneous and the details of this are discussed in Section 2.

et al. 2014). However, accretion might only be relevant early-on in disc galaxies before feedback and instabilities become dominant (see Elmegreen & Burkert 2010, and references therein). Ginzburg et al. (2022) found that accretion is unlikely the primary driver of turbulence in less massive haloes $< 10^{12}\,\mathrm{M}_{\odot}$ (at $z = 0$).

Several authors have developed analytic models of disc galaxies which incorporate $\sigma_{\mathrm{g}}$ and can thus be used to evaluate the source of galactic turbulence (e.g. Faucher-Giguère, Quataert & Hopkins 2013; Krumholz & Burkhart 2016; Hayward & Hopkins 2017; Krumholz et al. 2018; Orr et al. 2019; Nusser & Silk 2022), which usually focus on modelling one particular possible origin. Krumholz & Burkhart (2016) presented two galaxy-wide analytic models of galactic discs designed to reproduce the SFR–$\sigma_{\mathrm{g}}$ relation. One of their models is the analytic steady-state solution of a galactic disc derived by Krumholz & Burkert (2010), which is based on gravitational insta-bilities driving turbulence through radial inflows through the disc. They compare this model with a feedback-driven model by Faucher-Giguère et al. (2013), which assumes that the vertical gas pressure is balanced by the momentum input from supernovae explosions. Krumholz et al. (2018) extended this study by deriving a model that incorporates both effects, meaning that it can be applied to a wide diversity of galaxies. In recent years, several observational studies have applied these models to interpret observational data (Übler et al. 2019; Yu et al. 2019; Varidel et al. 2020; Girard et al. 2021; Yu et al. 2021). While such analytic models are efficient and useful for comparisons with data, they tend to involve a large set of free parameters that are not straight forward to constrain observationally.

Recent cosmological simulations have managed to reproduce the SFR–$\sigma_{\mathrm{g}}$ relation in disc galaxies over cosmic time (Hung et al. 2019; Orr et al. 2020; or the $\Sigma_{\mathrm{SFR}}$–$\sigma_{\mathrm{g}}$ relation in the case of Orr et al. 2020). Orr et al. (2020) showed that the most tenuous gas was also the most turbulent, which highlights the kinematic differences between gas phases. They also compared their simulations to analytic models

and concluded that both a feedback-regulated model and marginal (gravitational) stability can explain the turbulence in the neutral gas of their galaxies. However, these studies did not evaluate in detail the impact of observational artefacts on the SFR–$\sigma_{\mathrm{g}}$ relation.

In this paper, we present hydrodynamical simulations of entire disc galaxies of varying gas fractions and SFRs. We use these simulations to understand the roles played by stellar feedback and disc gravitational instability, as well as observational biases, in shaping the observed SFR–$\sigma_{\mathrm{g}}$ relation. The paper is organized as follows. In Section 2, we present the compilation of observational data considered in this work. In Section 3, we present the numerical code used for our simulations and how star formation and stellar feedback processes are implemented. In Section 4, we present the galaxy simulations and the emerging SFR–$\sigma_{\mathrm{g}}$ relation in each simulated galaxy. Having done so, we quantify the impact of beam smearing and the considered gas phases/tracers on the observed velocity dispersion. In Section 5, we evaluate modern analytic models of galactic disc turbulence compare to the hydrodynamical simulations, and discuss the caveats that exists when confronting them to observations. Finally, we carry out a stability analysis of the galaxies and demonstrate the ability of the $Q$ stability parameter to predict the simulated levels of turbulence. Our conclusions are summarized in Section 6.

## 2 OBSERVATIONAL DATA AND BIASES

Fig. 1 presents the observational data for the SFR and gas velocity dispersion ($\sigma_{\mathrm{g}}$) that we consider in this work. Each marker represents an individual galaxy[1] and is colour-coded according to the phase

---

[1]With the exception of data taken from Nguyen-Luong et al. (2016) who observed individual star-forming molecular clouds within the Milky Way.

of the gas tracer of $\sigma_g$; see Table A1 for references and general information about the observations. The left-hand panel shows the relation in semilog space (as is commonly done in the literature, e.g. Krumholz & Burkhart 2016; Krumholz et al. 2018), and the right-hand panel in log-space. The SFR–$\sigma_g$ relation is commonly considered to be well-described by a single power law, but as can be seen from the fitted (red) lines in the right-hand panel the relation better follows a piecewise power law which at low SFR goes as $\sigma_g \propto \mathrm{SFR}^{0.1}$ and steepens to $\sigma_g \propto \mathrm{SFR}^{0.4}$ at SFR $\gtrsim 2\,\mathrm{M}_\odot\,\mathrm{yr}^{-1}$. These fits show only an average slope of all the data and the relation may have further dependences, e.g. gas phase or scale.

There exists a number of important observational caveats related to this relation that need to be considered to form a more homogeneous data set that can be investigated into further detail. A disc galaxy observed at a high inclination will have its rotational motion almost directly along the line of sight (LoS), which widens the distribution of the observed radial velocities; thus, increasing the velocity dispersion. For observations at low spatial resolution, spectral features at different LoS velocities become blended. This is the cause of a known observational effect called *beam smearing*, which artificially increases the observed velocity dispersion, and is exacerbated for highly inclined galaxies where rotation blends together with turbulent motions.

Several codes have been developed to correct for beam smearing by modelling a typical galaxy and reconstructing its rotation curve and kinematics (e.g. ROTCUR, GALFIT, TiRiFiC, DYSMAL, 3D-Barolo; van Albada et al. 1985; Peng et al. 2002; Józsa et al. 2007; Davies et al. 2011; Di Teodoro & Fraternali 2015, respectively). The methods used vary between the codes, which can significantly affect the derived velocity dispersion. In particular, methods based on 2D modelling are biased towards higher $\sigma_g$ values (see the discussion in Di Teodoro & Fraternali 2015), which Rizzo et al. (2021) highlighted as an underprediction of $V/\sigma$. Assuming a constant velocity dispersion throughout the disc has also been shown to lead to a bias towards higher $\sigma_g$ estimate (see the discussion in Rizzo et al. 2021). Instead, 3D models (making use of datacubes) need to be employed to accurately correct for beam smearing. Furthermore, disc modelling of near edge-on or thick discs, where the line of sight overlaps the disc several times, results in ambiguous velocity dispersions. At low inclinations ($<40°$), tilted-ring models might have significant residual error due to the difficulty of disentangling the rotational velocity and the velocity dispersion (Kamphuis et al. 2015).

Observational data from high-redshift galaxies ($z \gtrsim 1$) suffer from poor spatial resolutions. This makes comparison between observational data of turbulence in high-redshift and local galaxies troublesome, due to possible scaling relations between turbulence and the observed scale. Galaxy observations exploring the scaling between $\sigma_g$ and spatial resolution report conflicting results and are not conclusive, but on average an increase in $\sigma_g$ is expected with an increase of scale (see Elmegreen & Scalo 2004, and references therein). We explore the role of observed scale in Section 4.2.1 and find that for a wide range of scale, if the galaxy is not inclined, $\sigma_g$ differs by a factor of, at most, 2. However, if the galaxy is highly inclined ($>60°$), and if this inclination is unaccounted for, patch size could have a major impact; even sufficient to explain the entire SFR–$\sigma_g$ relation! Furthermore, lower resolution naturally means fewer data points, which complicates the fitting process used in beam smearing corrections. Due to the range of orbital velocities present over a large spatial scale, the velocity field cannot be accurately retrieved at high redshifts (Epinat et al. 2009). However, even at low redshifts beam smearing may have a substantial effect on $\sigma_g$

from galaxies with a high SFR (Varidel et al. 2016). Kohandel et al. (2020) employed cosmological simulations and identified that if beam smearing is not accounted for in high-$z$ galaxies, the velocity dispersion can be overestimated by as much as over a factor of 2.

In the literature, $\sigma_g$ tends to be reported as a weighted average of the velocity dispersion calculated in each element (i.e. pixels), and then used to represent the entire galaxy; along with a galaxy-wide SFR, which is simply the sum of SFR from each pixel. Several different weights have been used in this regard: flux (e.g. Lemoine-Busserolle et al. 2010; Wisnioski et al. 2011; Varidel et al. 2016), luminosity (e.g. Davies et al. 2011; Moiseev et al. 2015) and errors from emission line fitting (Epinat et al. 2009). Lehnert et al. (2013) briefly evaluated the significance in weighing with the surface (H$\alpha$) brightness, signal-to-noise, and flux, but found that the resulting $\sigma_g$ were consistently only $\sim 10$ per cent higher than the non-weighted mean. Several authors have suggested that a flux-weighted average favours the inner, more luminous, regions of galaxies (Davies et al. 2011; Di Teodoro, Fraternali & Miller 2016). These regions are also highly turbulent, which may result in brightness- or SFR-weighting yielding a bias towards large $\sigma_g$. Furthermore, these inner regions are also more prone to be beam smeared, due to the steeper rotational curve velocity near the galaxy centre (e.g. Józsa et al. 2007).

As mentioned in Section 1, the ISM has distinct gas phases with different dynamics. Thus, data from different observational tracers cannot be directly compared, as the velocity dispersion of each phase cannot be connected in a straightforward manner through theory. For example, Fig. 1 shows a clear offset of the H$\alpha$ observational data at low SFRs (the yellow squares) when compared to other tracers. Different gas tracers could then trace separate parts of the SFR–$\sigma_g$ relation. This is further discussed in Section 4.2.3.

There is no universally accepted method to measure the velocity dispersion in galaxies, and it is thus difficult to form a completely homogeneous data set. For example, most authors have measured $\sigma_g$ within individual pixels and then determined a weighted mean (e.g. Epinat et al. 2009; Lemoine-Busserolle et al. 2010; Di Teodoro et al. 2016; Girard et al. 2021), while some (e.g. Lehnert et al. 2013) have determined $\sigma_g$ from the integrated spectra (summing up all spectra before fitting the line width). The first method to some extent corrects for rotation and reduce (but do not eliminate) the effect of beam smearing. Others still have employed (empirical) models combined with observational data to determine $\sigma_g$ (e.g. Cresci et al. 2009). Epinat, Amram & Marcelin (2008) reported the dispersion in radial velocity, rather than line-of-sight velocity, from their best-fitting disc models (essentially the kinematic residuals of a well-behaved disc). The difference in method deployed by authors might give rise to systematic differences in $\sigma_g$ (e.g. Lehnert et al. 2013, attain $\sigma_g$ $> 150\,\mathrm{km\,s^{-1}}$, significantly higher than found by Cresci et al. 2009; Lemoine-Busserolle et al. 2010 with similar data). Furthermore, there is a wide range of morphologies and galactic properties in the set of data we compare with here, as it contains local, high-redshift, and dwarf galaxies. However, understanding these differences is important to correctly utilize the observational data.

## 3 NUMERICAL METHOD

In this work, we perform hydrodynamic + $N$-body simulations of entire galactic discs using the Adaptive Mesh Refinement (AMR) code RAMSES (Teyssier 2002). The code solves the Euler equations for the fluid dynamics using the Godunov scheme assuming an ideal monoatomic gas with an adiabatic index $\gamma = 5/3$. Stars and dark matter are represented by collisionless particles. The accelerations of the particles and gas are computed from the gravitational potential, via

**Table 1.** Characteristics of each simulation. Refinement time refers to the time allowed for the initial conditions to relax, after which the refinement/resolution is increased.

| Name of run | $f_g$ (per cent) | Feedback? | $\epsilon_{ff}$ (per cent) | Refinement time (Myr) | SFR[a] ($M_\odot$ yr$^{-1}$) |
|---|---|---|---|---|---|
| fg10_noFB | 10 | No | 1 | 200 | 4 |
| fg10_FB | 10 | Yes | 10 | 200 | 1 |
| fg50_noFB | 50 | No | 1 | 100 | 100 |
| fg50_FB | 50 | Yes | 10 | 100 | 25 |

[a]50 Myr after refinement.

the Poisson equation, using the multigrid method (Guillet & Teyssier 2011) at each refinement level. Metal-dependent gas cooling follows the tabulated cooling functions of Sutherland & Dopita (1993) for $T > 10^4$ K and Rosen & Bregman (1995) for lower temperatures.

### 3.1 Star formation and stellar feedback

The adopted star formation and feedback physics is presented in Agertz et al. (2013, see also Agertz, Romeo & Grisdale 2015), which we briefly summarize here. Star formation is treated as a Poisson process, sampled using $10^3$ $M_\odot$ star particles on a cell-by-cell basis according to the star formation law,

$$\dot{\rho}_\star = \epsilon_{ff} \frac{\rho}{t_{ff}} \text{ for } \rho > \rho_\star, \quad (1)$$

where $\rho$ is the gas density, $\rho_\star = 100 \, m_H$ cm$^{-3}$ is the adopted density threshold, $t_{ff} = \sqrt{3\pi/32G\rho}$ is the free-fall time of a spherically symmetric cloud and $\epsilon_{ff}$ is the star formation efficiency per free-fall time. In the simulations including stellar feedback, we adopt $\epsilon_{ff} = 10$ per cent, which has been shown to be able to reproduce the properties of ISM and giant molecular cloud populations, as well as observed $\epsilon_{ff}$. In the absence of star formation regulation via feedback, we adopt a lower $\epsilon_{ff} = 1$ per cent as it better captures the mean $\epsilon_{ff}$ in giant molecular cloud populations (see Grisdale et al. 2017, 2018, 2019). Each formed star particle is assumed to be a simple stellar population with a Chabrier (2003) initial mass function.

Central to our study is the ability of stellar feedback to drive ISM turbulence. The feedback model treats the time-dependent injection of momentum, energy, mass, and heavy metals[2] from supernovae (SNe) type Ia and type II, stellar winds and radiation pressure (see Agertz et al. 2013, for details). SNe are treated as discrete events (Agertz et al. 2015). To robustly capture the effect from SNe, which is the dominant source of feedback in terms of momentum and energy input, we follow Kim & Ostriker (2015, see also Martizzi, Faucher-Giguère & Quataert 2015) and inject the terminal SN momentum to ambient cells when the cooling radius is resolved by less than six cells.

### 3.2 Simulation suite

The initial conditions are based on those of the isolated disc galaxy in the AGORA project (Kim et al. 2014, 2016), set up to approximate a Milky Way-like galaxy following the methods described in Hernquist (1993) and Springel (2000). Briefly, we adopt an NFW dark matter halo (Navarro, Frenk & White 1996) with a concentration parameter $c = 10$ and virial circular velocity $v_{200} = 150$ km s$^{-1}$. This translates into a halo virial mass $M_{200} = 1.1 \times 10^{12}$ $M_\odot$ within $R_{200} = 205$ kpc. The total baryonic disc mass is $M_{disc} = 4.5 \times 10^{10}$ $M_\odot$ with a gas

[2]We track iron (Fe) and oxygen (O) abundances separately, see Rhodin et al. (2019).

fraction that we vary, as described below. The initial stellar and gaseous components follow exponential surface density profiles with scale lengths $r_d = 3.4$ kpc and scale heights $h = 0.1r_d$. The bulge-to-disc mass ratio is 0.125. The bulge mass-profile follows a Hernquist profile (Hernquist 1990) with scale length $0.1r_d$. The dark matter halo and stellar disc are represented by $10^6$ particles each and the bulge consists of $10^5$ particles.

In this work, we are interested in modelling the evolution of high redshift and local disc galaxies. The key parameter that evolves over time and sets several important characteristics (e.g. star formation) of a galaxy is its gas fraction. By varying the initial gas fraction, at a fixed total disc mass, in the initial conditions, we model a 'low-redshift' galaxy, with $f_g = 10$ per cent, and the 'high-redshift' counterpart, with $f_g = 50$ per cent (see van Donkelaar, Agertz & Renaud 2022, for an explicit approach). These models are not necessarily analogues of the same galaxy, but they still capture the environment inside galaxies at different evolutionary stages.

Both gas fractions are simulated with and without stellar feedback processes (see Table 1 for details). This allows us to constrain the degree to which feedback or galaxy self-gravity drive ISM turbulence (see also Agertz et al. 2009). The galaxies are simulated in isolation, i.e. without cosmological context, in order to understand how ISM turbulence is driven by internal effects rather than environmental effects such as galaxy interactions and gas accretion. These additional effects perturb the morphology and kinematics of the disc and, thus, the stability and evolution of the disc. In particular, Hafen et al. (2022) showed that the formation of thin discs, which are inherently less turbulent, is unfavourable when accretion is dominated by cold filaments.

We begin by evolving the initial conditions at low spatial resolution ($\Delta x \approx 150$ pc) for 100–200 Myr (see Table 1) in order for them to relax and the galaxy to develop spiral structure. After this epoch of letting the galaxies relax, we allow for maximum refinement and activate stellar feedback. Our analysis is done on the data outputs from the start of this refinement period until 200 Myr after, with a time between outputs of 5–25 Myr. We allow for the adaptive mesh to refine to a maximum of 16 levels, corresponding to a spatial resolution of $\Delta x \gtrsim 9$ pc.

### 3.3 Measuring the velocity dispersion and star formation rate

In order to simplify the comparison to literature data where galaxy-wide values for $\sigma_g$ and the SFR are frequently reported, we calculate these quantities within local patches and then combine these into global (galaxy-wide) averages. Patches allow us to evaluate how ISM properties depend on the observational resolution of specific observations, and hence physical scale – an important concept in astrophysical turbulence (e.g. Mac Low & Klessen 2004; Kritsuk et al. 2007; Grisdale et al. 2017). Global quantities are particularly relevant in high-$z$ surveys where the spatial resolution becomes comparable to the size of the galaxy (as discussed in Section 2).

The local patches are analogue to a single resolution element of an observation, i.e. a pixel or spaxel, and are here defined as a set of cylindrical beams with diameters ranging between 0.1 and 10 kpc. The patches are distributed uniformly in the radial direction and with the same angular separation. Thus, the number of patches are concentrated near the galactic centre, the region of interest when investigating high SFRs and $\sigma_g$. When investigating the effects of galaxy inclination, the beams were inclined relative to the disc plane according to our choice of observed line-of-sight angles: (0°, 15°, 30°, 45°, 60°, 75°, 90°). The local set-up then produces ~1000 patches for each output (before rejecting unusable patches, i.e. with no gas mass or no star formation).

Each patch covers several simulation cells. Every local quantity was calculated by summing or averaging the values of each simulation cell within a patch. Thus, the local SFR was calculated as the sum of SFR of all cells within a patch. The SFR within a patch was in turn calculated by binning the stellar ages of stars in bin sizes of 10 Myr (motivated by the lifetime of H II regions), then calculating the difference in stellar mass between adjacent time bins and dividing by the bin size.

Furthermore, we calculated the local $\sigma_g$ as the mass-averaged radial (along LoS) velocity dispersion within a patch, which represents the turbulence of the majority of the gas mass. However, this is only the pure turbulent motion $\sigma_{g,turb}$ and does not account for the unresolved motion of the gas. Thus, the speed of sound in the medium $c_s = \sqrt{\frac{\gamma k_B T}{m_H}}$ was added in quadrature to the velocity dispersion, $\sigma_g = \sqrt{\sigma_{g,turb}^2 + c_s^2}$. The sound speed is on the order of a few km s$^{-1}$ for molecular and neutral hydrogen, and 10–15 km s$^{-1}$ for ionized gas.

The global average of the velocity dispersion was computed as a mass-weighted average of the local patches. As with observations, the patch size was fixed and we chose to set $d_{patch} = 2$ kpc, which represents the spatial resolutions of observed, resolved, galaxies at $z \sim 1$–2 (see Table A1). Varying the patch size by 1–2 kpc does not alter the results significantly. The global SFR is simply the sum of SFR of all patches within the galactic disc.

We present our global averages in the coming figures as the mass-weighted mean value of the global averages calculated for the galaxy at different times and include the variation in both $\sigma_g$ and SFR as error bars. We chose to weight $\sigma_g$ by the gas mass of the corresponding phase since the mass is directly correlated to emission lines originating from the gas and is thus a good proxy for radiation flux.[3] However, we find no significant difference between weighting global H$\alpha$ velocity dispersions with mass, emissivity, or SFR. At most, SFR-weighting yields $\sim$ 10 per cent higher $\sigma_g$ in the feedback runs compared to mass-weighting or applying no weights. In Section 4.2.3, we perform mock observations of certain gas phases and go more into depth about phase-specific weights.

## 4 RESULTS

We begin our analysis by visualizing the simulations in Fig. 2. Shown is the mass-weighted mean gas density and temperature 50 Myr after the initial refinement period (see Section 3.2). All simulated galaxies feature a turbulent, irregular ISM. Cold dense star forming

clumps can be found in all simulations, but are most prominent when feedback is absent. In the high gas fraction models, the clouds dominate the galaxy's morphology, in agreement with observations of high-redshift galaxies (e.g. Elmegreen et al. 2007, 2009; Genzel et al. 2011; Zanella et al. 2019). At this time, the galaxies with feedback produce stars at a rate of $\sim$ 25 and $\lesssim$ 1 M$_\odot$ yr$^{-1}$ for the `fg50_FB` and `fg10_FB` runs, respectively, whereas the galaxies without any feedback produce 4–5 times more stars.

Stellar feedback disrupts the dense star forming clouds and creates regions filled with hot gas in the ISM. The effect of feedback is also evident from the thickened disc structure in the vertical projection. In `fg50_FB`, vigorous galactic outflows are present, with cold gas entrained out to 10 kpc above the disc mid-plane, as observed in local starburst galaxies (see e.g. Veilleux, Cecil & Bland-Hawthorn 2005, for a review). While stellar feedback impacts the gaseous morphology of the galaxy, it is not clear how this manifests itself in terms of observed gas velocity dispersions, globally and locally, across different gas tracers. Quantifying this is the focus of the sections below.

### 4.1 The SFR–$\sigma_g$ relation

With the morphology and behaviour of the galaxy outlined, we now focus on the SFR–$\sigma_g$ relation. We begin by analysing the simulated galaxies completely face-on, without any influence of observational artefacts such as beam smearing, which we investigate in Section 4.2. Fig. 3 shows SFR–$\sigma_g$ relation for both simulated galaxies, with and without feedback, compared to the set of observational data. The local quantities (computed in patches, defined in Section 3.3) are represented by contours, indicating the intervals in which 30, 68, and 80 per cent of the data is contained. The global quantities are represented by markers with error bars covering the entire distribution of the global averages.

The plot shows an overall agreement in the SFR–$\sigma_g$ relation between observations and simulations for the relevant range in SFRs. A striking result it that the presence of stellar feedback does not significantly impact the simulated SFR–$\sigma_g$ relation, with only a broadening of the $\sigma_g$ distribution in the feedback case. The source of this broadening is the formation of the more turbulent warm ionized phase, primarily caused by supernovae, which we investigate further in Section 4.2.3.

Furthermore, the simulations are able to reproduce two recognizable features of the observational data: the plateau at $\sigma_g \sim$ 10–20 km s$^{-1}$ for SFR $\lesssim$ 2 M$_\odot$ yr$^{-1}$ and the steep increase of $\sigma_g \sim$ 60 km s$^{-1}$ for SFR $\gtrsim$ 2 M$_\odot$ yr$^{-1}$. The galaxy-wide $\sigma_g$ and SFR also match well with observational data, regardless of the adopted weighting scheme (see Section 3.3). However, none of our simulations are able to recover the large observed turbulent velocity in excess of $\gtrsim$ 60 km s$^{-1}$, as reported by many studies, including analytical work (e.g. Krumholz & Burkhart 2016; Krumholz et al. 2018). While this in principle could be remedied by modelling galaxies with even higher gas fractions and hence SFRs (but see Renaud, Romeo & Agertz 2021), this discrepancy can arise by not accounting for a number of key observational effects, which we explore next.

### 4.2 Observational effects

As discussed in Section 2, the observational data available to probe the SFR–$\sigma_g$ relation is very heterogeneous and, even within the same survey, galaxies are observed at different spatial resolutions and inclinations. While inclination corrections are commonly done, even minor residual errors can impact the derived turbulent velocities

---

[3]We note that there is no consensus in literature on what weights should be applied when combining patches to calculate global values (see Section 2), but we elect to compare with flux-weighting as it is one of the most common approaches and, thus, allows for a better comparison with literature data.
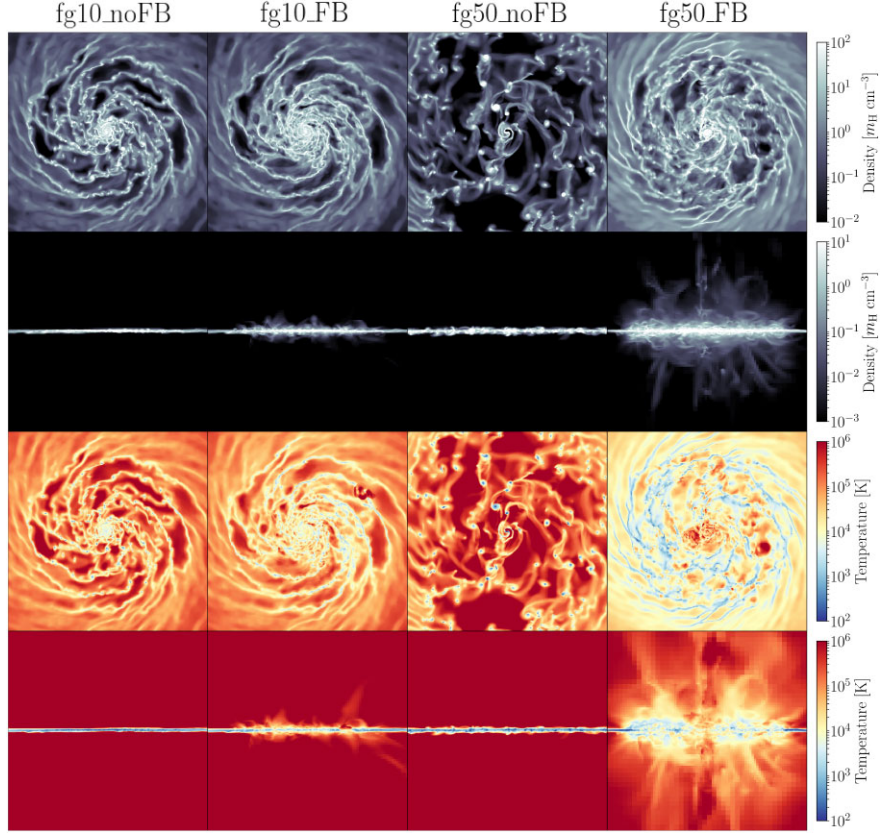
**Figure 2.** The gas density and temperature in the simulated galaxies. The parameters were taken as the mass-weighted average of the cells along line of sight (face- and edge-on). The size of the boxes are 20 kpc × 20 kpc, and calculated 50 Myr after feedback was turned on. The runs without any feedback are seen to form dense clumps of gas and there is a clear correlation with the denser areas being colder. Some clumping, as seen in the fg50_FB run, is expected in high-redshift galaxies. Violent gas outflow caused by feedback are observed from the side views and is more prominent in the more gaseous disc.
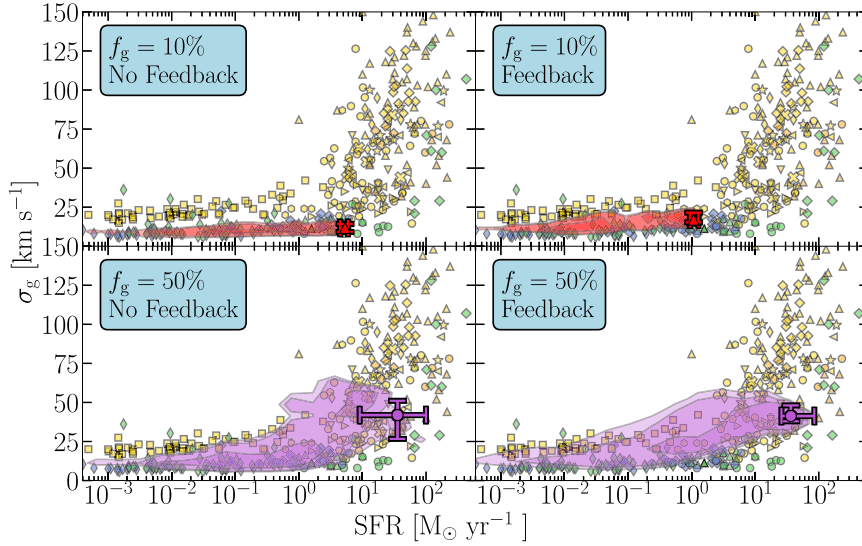


**Figure 3.** The SFR–$\sigma_g$ relation for the galaxy simulation. The markers correspond to the literature data in Table A1. The simulation data using a patch approach are presented as a coloured contour and the global averages are shown as markers with error bars, as described in Section 3.3. The simulation data shown here are for no inclination, uses patch sizes ≥1 kpc, and includes all of the gas (regardless of phase). A remarkable agreement between simulations and observations can be seen and the simulations reproduce two distinct properties of the SFR–$\sigma_g$ relation: the plateau at SFR ≲ 2 $M_\odot$ yr$^{-1}$ and (in the high gas fraction galaxy) the steep increase at higher SFRs. Feedback does not have a significant impact on the overall $\sigma_g$, but we notice a higher dispersion in the values of $\sigma_g$ for all SFRs; this is related to the formation of the warm ionized phase (discussed in detail in Section 4.2.3).
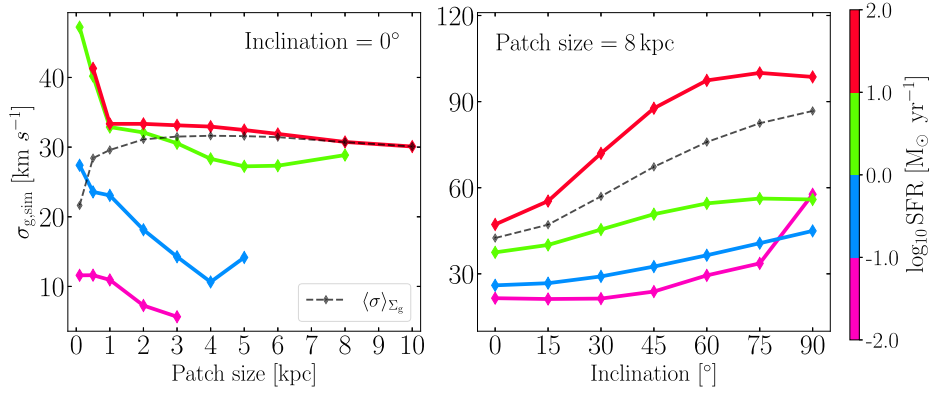
**Figure 4.** The gas velocity dispersion in a range of SFR bins (according to the colourbar) as a function of the patch size (left) and the inclination angle (right). This figure shows simulated data from fg50_FB, but the same relations are found for all simulation runs. The increase for smaller patch sizes in each individual SFR bin is purely due to $\Sigma_{SFR}$ increasing with decreasing patch sizes. The surface density-weighted average (dashed line) shows the negligible effect of patch size on the calculated $\sigma_g$. Furthermore, beam smearing severely impacts $\sigma_g$, especially for large SFRs.

(see the discussion in Section 2). Furthermore, various gas tracers are used in the literature and it is not clear that these are directly comparable, given their vastly different origin, density, etc. Our first task is thus to unpack these observational artefacts and determine their potential effect on the SFR–$\sigma_g$ relation.

### 4.2.1 Role of scale

In order to quantify the effects of scale on the velocity dispersion, we analyse $\sigma_g$ as a function of patch size at fixed SFR. The relations are shown on the left-hand panel of Fig. 4 for fg_50FB, which is analysed face-on. As expected, there is a clear sequence in terms of SFR and $\sigma_g$, with higher SFR bins hosting higher levels of turbulence. We also notice a negative correlation between the size of the patch and $\sigma_g$, for fixed values of SFR, most pronounced for SFR $\lesssim 1$ M$_\odot$ yr$^{-1}$. This may seem counter-intuitive given the positive correlation between velocity dispersion and size observed for molecular clouds[4] (e.g. Larson 1981; Heyer et al. 2009). This is a direct consequence of the SFR binning, as smaller patches with the same SFR have higher surface density of star formation ($\Sigma_{SFR}$), which results in higher levels of turbulence, in agreement with observations (see Appendix B). We find the same behaviour is in all simulated galaxies, regardless of the inclusion of stellar feedback or not.

When computing a mass-weighted average velocity dispersion of patches as a function of scale, we recover $\sigma_g \sim 30$ km s$^{-1}$ for all scales above $\sim 1$ kpc. We note that all observations considered in this work (see Table A1) have spatial resolution $\gtrsim 500$ pc. The range of different scales present in the observations should therefore not greatly impact the inferred SFR–$\sigma_g$ relation, if the galaxy is observed nearly face-on.

In one of the coming sections, we will show that the turbulence induced by stellar feedback is most directly detected in the ionized gas, traced by recombination lines. Feedback is believed to insert most of its turbulent energy at scales around the disc scale height (sub-kpc scale). We analyse further the velocity dispersion in the smallest scales we probe (0.1, 0.2, and 0.5 kpc) within neutral, molecular, and ionized gas. In the presence of feedback, the neutral and molecular

gas both show a noticeable increase in velocity dispersion at scales $\leq$ 0.5 kpc near regions with low SFR, compared to when no feedback is present. This is due to the injection of turbulent motion, by feedback, into neighbouring regions with low SFR. Furthermore, ionized gas in high SFR regions is significantly more turbulent at $\leq 0.5$ kpc when feedback is present, which indicates that feedback might have a significant impact at sub-kpc scales. Our analysis reveals that the impact of feedback at various scales is complex and heavily depends on numerous factors specific to the environment observed. We leave disentangling the details of this as future work.

### 4.2.2 Role of beam smearing/inclination

To understand the role of beam smearing (discussed in Section 2), we measure the LoS $\sigma_g$ in patches of size 8 kpc in fg50_FB for galaxy inclination angles $\theta = 0-90°$. Analogous to the previous section, we compute $\sigma_g$ for fixed values of SFRs as well as a mass-weighted average velocity dispersion. The results are shown in the right-hand panel of Fig. 4. The effect of the inclination angle is a strong function of the SFR, with $\sigma_g$ increasing by more than a factor of 2, and reaching $\sigma_g > 100$ km s$^{-1}$ for the highest SFR bin ($\gtrsim 10$ M$_\odot$ yr$^{-1}$, red solid line) when the galaxy is inclined by $\theta \sim 60°$. This effect is expected, as the SFR increases towards the galaxy centre where the rotation curve varies strongly with galactocentric radius. Beam smearing is here most severe for large observational patches, as velocity gradients become less resolved which broadens the velocity distribution and consequently the observed LoS $\sigma_g$.

The fact that the effect of beam smearing becomes less pronounced at low SFRs has a significant impact on the resulting SFR–$\sigma_g$ relation, as seen in Fig. 5. Here each panel features, from left to right, measurements for $\theta = 0°$, $\leq 30°$, and $\leq 60°$ for patch sizes $\geq 4$ kpc. The joint effect of higher $\sigma_g$ at high inclination angles and high SFR, identified above, leads to the simulated SFR–$\sigma_g$ relation matching the observed trend, even up to values as large as $\sigma_g \sim 140$ km s$^{-1}$ when including galaxy inclinations up to $60°$ (right-hand panel). To demonstrate the impact of beam smearing on observed scales, we plot the SFR–$\sigma_g$ relation with patch sizes of 0.5, 1, 2, 4, 8 kpc for inclinations $\theta \leq 60°$ in Fig. 6. This figure highlights how low observational resolution may result in severe beam smearing of the observed kinematic of gas in disc galaxies.

This striking agreement suggests that insufficient inclination correction, and the accompanied beam smearing, in principle can

---

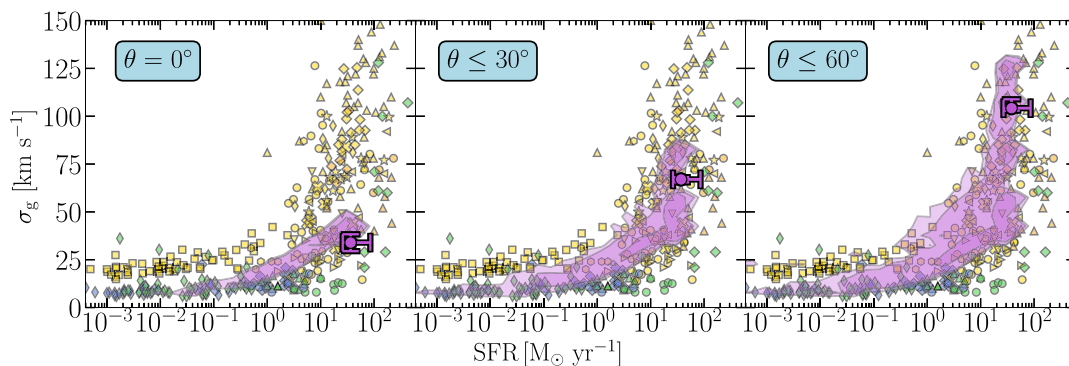[4]Note however that the Larson scaling relations are only valid on scales $\lesssim 100$ pc.

**Figure 5.** The SFR–$\sigma_g$ relation for three particular ranges of disc inclinations, using data from the `fg_50FB` simulation. The simulation data using a patch-approach are presented as a coloured contour and the global averages are shown as markers with error bars, as described in Section 3.3. The leftmost panel assumes that all galaxies are viewed head-on, while the other panels depict how the relation would look for a mixture of galaxy inclinations with $\theta \leq 30°$ and $\theta \leq 60°$. The global averages use the inclination $\theta = 0°$, $30°$, $60°$, respectively. Beam smearing is clearly increasing the $\sigma_g$ along LoS. Beam smearing is seen to affect patches with high SFR significantly more, but there is likely hidden variables here: the inner regions and larger patch sizes (see Section 4.2.2 for details).
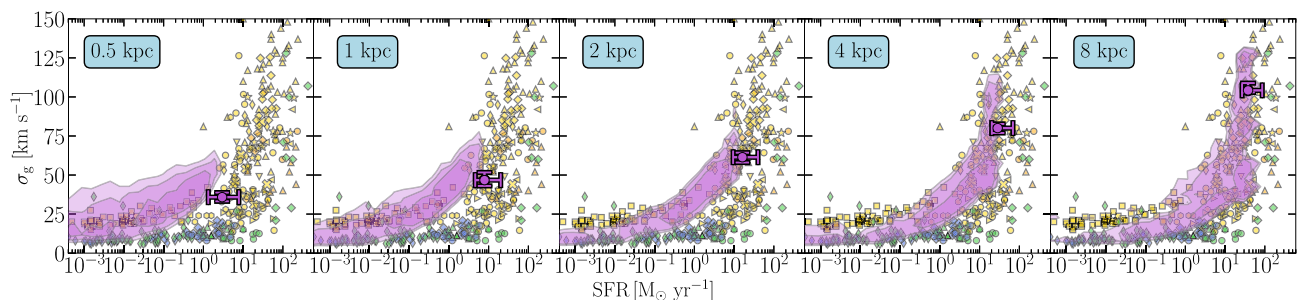


**Figure 6.** The SFR–$\sigma_g$ relation for various patch sizes. The simulation data using a patch-approach are presented as a coloured contour and the global averages are shown as markers with error bars, as described in Section 3.3. The data shown here are of `fg50_FB` with an inclination of $\theta \leq 60°$ (global averages use $\theta = 60°$). The observed velocity dispersion drastically increases with larger patch sizes, which highlights the significance of beam smearing for poorly resolved observations of galaxies. As the data are highly heterogeneous, most of the high SFR data come from poorly resolved high-$z$ galaxies.

explain the highest values of $\sigma_g$ observed for rapidly star forming galaxies. The sensitivity to even mild inclination effects (e.g. $\theta \leq 30°$ in Fig. 5) illustrates the difficulty in recovering the true turbulent $\sigma_g$, especially for poorly resolved high-redshift galaxies that feature highly clumpy morphologies and/or are undergoing interactions.

We note that most observational data presented in this work have been corrected for inclination (see Table A1). Therefore, while some of these high $\sigma_g$ can be explained as uncertainties on the galaxy's inclination, it remains to be seen whether this explanation holds in the general case. We note that the galaxies with the highest SFRs and $\sigma_g$ are all high-redshift galaxies observed in H$\alpha$. How the kinematics of this specific gas tracer differs from local tracers of molecular gas (CO) and H I, and whether this can bias the SFR–$\sigma_g$ relation, is investigated next.

### 4.2.3 Mock observations and role of gas phase

To allow for a closer comparison to observations, we next evaluate the turbulent motions for different gas tracers. Because gas phases have different characteristic densities and temperatures, their kinematics are likely to differ. This in turn complicates the simple, and common, interpretation of the observed SFR–$\sigma_g$ relation as a unique relation for all gas phases. For our analysis, we consider the molecular H$_2$ gas phase (observationally traced by CO) by calculating the

molecular gas fraction (following Krumholz, McKee & Tumlinson 2009), the neutral (atomic) hydrogen phase (traced by H I) from the hydrogen number density, and the warm ionized phase (traced by H$\alpha$) from the H$\alpha$ emissivity (following the process detailed in Appendix C).

A map of the gas density in each phase of the two simulations with feedback (`fg10_FB` and `fg50_FB`) are shown in Fig. 7. The lower gas fraction galaxy is found to have a less turbulent medium, with most of the molecular and atomic gas being concentrated into its spiral arms with very little outflows seen in the edge-on view. The higher gas fraction galaxy features massive molecular gas clumps and much more intense outflows. The central 10 kpc are dominated by molecular gas (embedded in ionized H$\alpha$ gas) with the atomic gas phase being much more diffuse than in the low gas fraction galaxy. Both simulations feature distinct hot ionized bubbles in the H$\alpha$ gas tracer, which are indicative of feedback driven bubbles beginning to cool down.

Next we evaluate the SFR–$\sigma_g$ relation for the three gas phases, plotted in Fig. 8 for all simulations. The observational data in the plots are the same as previous SFR–$\sigma_g$ graphs, but each panel now exclusively shows observational data for a specific gas tracer. The simulation data are here presented as weighted global averages (as explained in Section 3.3, using the same weights as for the maps). The figure shows that each simulated gas phase matches well with the corresponding observational data. As before, this is the case regardless of the presence of stellar feedback, but here feedback has
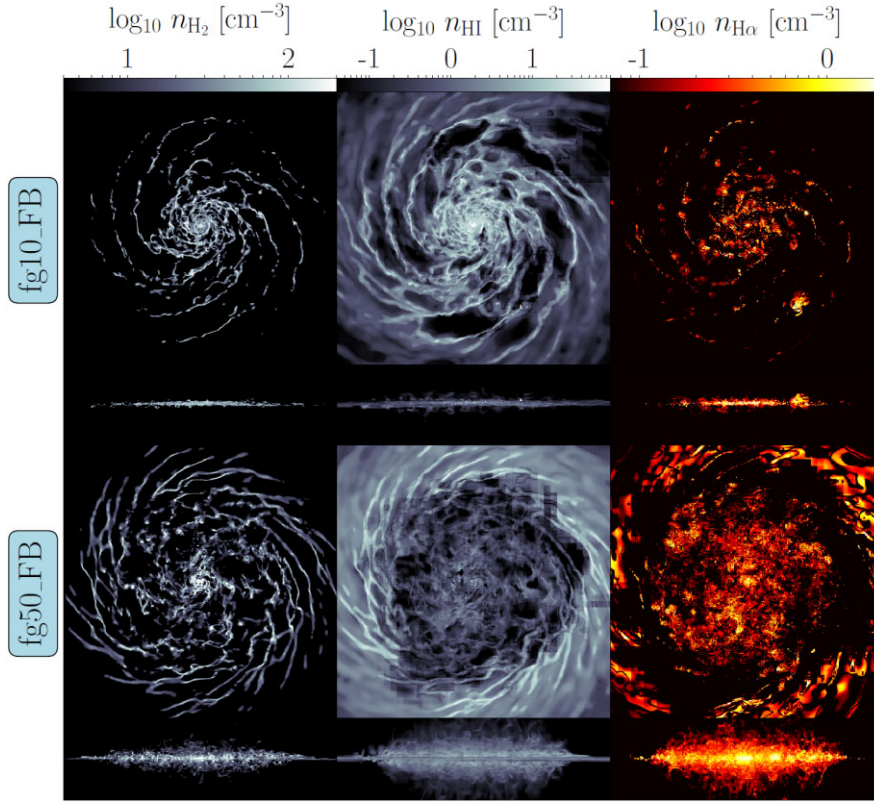
**Figure 7.** The mean gas number density $n$ weighted by parameters related to each phase of the different gas phases/tracers considered ($H_2$, H I, and H $\alpha$; see Section 4.2.3). The two simulations with feedback ($f_g = 10$ per cent, 50 per cent) are shown 100 Myr after feedback has been activated. The spatial size of the larger boxes is 25 kpc (8 kpc height for the smaller box) and each pixel of the image is 25 pc. Notably, the molecular gas is confined within the arms and individual, massive, gas clumps. The atomic (H I) gas is more evenly spread. The H $\alpha$ tracer shows the formation of warm ionized shells, which is a consequence of stellar feedback, and highlights its impact on the ISM.

a large impact on the velocity dispersion of the ionized gas phase, which we detail below.

Furthermore, the figure demonstrates that the turbulence is very different between different phases. The way in which the SFR and $\sigma_g$ are related is hence not (theoretically) captured by models unless they are designed for individual gas phases that can be compared to the corresponding observational data. In particular, most observational data at high SFRs and high $\sigma_g$ are high-redshift galaxies in H $\alpha$. Our simulations including stellar feedback indicate that this gas phase features significantly higher levels of turbulence ($\sigma_g > 100\,\mathrm{km\,s^{-1}}$) compared to the neutral ISM ($\sigma_g < 40\,\mathrm{km\,s^{-1}}$) at a given SFR (see yellow symbols in Fig. 8). As such, H $\alpha$ observations are likely biased towards high $\sigma_g$ values in the SFR–$\sigma_g$ relation. This property was recently highlighted by Girard et al. (2021), who found that galaxies probed with H $\alpha$ data in the DYNAMO and EDGE-CALIFA surveys had roughly 2.5 times higher $\sigma_g$ than the neutral gas, in close agreement with our findings for the simulation including stellar feedback. The EDGE-CALIFA survey of local galaxies (Levy et al. 2018) showed a difference between molecular and ionized velocity dispersion of a factor of roughly 2. However, some studies have suggested that galactic turbulence in ionized and molecular gas are similar (e.g. Übler et al. 2018; Molina et al. 2019, 2020). This discrepancy might be due to the observations tracing outflows, rather than the turbulent motions within the ISM, or beam smearing.

The H $\alpha$ gas tracer is hence the one gas phase where we expect to find a strong signature of the effect of stellar feedback, which is required to recover $\sigma_g \sim 100\,\mathrm{km\,s^{-1}}$. Furthermore, only a small fraction ($\sim 10$ per cent) of the available turbulent kinetic energy

needs to couple to the diffuse H $\alpha$-traced gas phase in order to explain these values (see Appendix D). Without feedback in the galaxy, the velocity dispersion never exceeds $\sigma_g \sim 50\,\mathrm{km\,s^{-1}}$.

## 5 DISCUSSION

### 5.1 Comparison to analytic models

We now turn to comparisons with analytic models from the literature to ascertain their potential to reproduce the observed SFR–$\sigma_g$ relation. Such models are useful and fast ways for studying the physics of galactic turbulence driving, such as gravitational instability and stellar feedback. Direct comparisons to full hydrodynamical simulations are beneficial for understanding any possible caveats to the simplifications made in such models. We focus on the models presented by Krumholz et al. (2018, hereafter KBFC18) (see also Krumholz & Burkert 2010; Krumholz & Burkhart 2016, for earlier work) as their formalism has successfully been applied to many observational surveys of star-forming galaxies (including Übler et al. 2019; Yu et al. 2019, 2021; Varidel et al. 2020; Girard et al. 2021). Most of these surveys use recombination lines and, thus, trace the ionized gas phase, which we find is more turbulent than the cold dense gas driving gravitational instability.

Gravitational instabilities in KBFC18 are quantified by the $Q$ stability parameter. We will return to this topic in Section 5.2, but for now it suffices to note that under the approximation of an infinitesimally thin disc, this parameter for an individual galactic
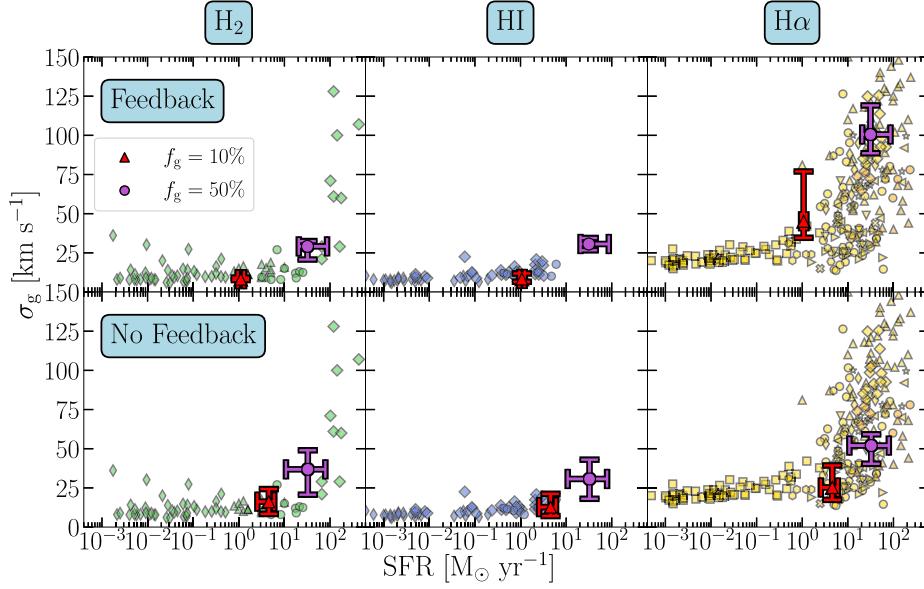
**Figure 8.** The SFR–$\sigma_g$ relation for the three distinct gas phase. The upper panels show the results from the simulations with feedback and the lower panels show for those without any feedback. The $\sigma_g$ of each phase is evaluated using phase-specific weights, as detailed in Section 4.2.3. The simulations agree strikingly well with the observational data, with the exception of high SFR regions in the H I and H $\alpha$, where there is no data due to observational limitations. Particularly, the high $\sigma_g$ observed with the H$\alpha$ tracer is retrieved in the simulation data.

component (gas or stars) reads

$$Q_i = \frac{\kappa \sigma_i}{\pi G \Sigma_i}, \qquad (2)$$

where $\kappa$ is the epicyclic frequency, $\sigma$ is the radial velocity dispersion, and $\Sigma$ is the surface density [see Safronov 1960; Goldreich & Lynden-Bell 1965, on the parameter for fluids ($i = g$), and Toomre 1964 on that for stars ($i = \star$)]. Galactic discs are traditionally regarded as stable if $Q_i \geq 1$. Note, however, that this stability criterion neglects the gravitational coupling between stars and gas, the vertical structure of the disc, the effect of non-axisymmetric perturbations, and other important factors (for an overview, see section 5.2 of Romeo & Fathi 2015 and section 4.2 of Romeo & Fathi 2016). The actual stability threshold is significantly higher: $Q \approx 2$–3 (e.g. Romeo & Mogotsi 2017), especially at high gas fractions (as we will show in Section 5.2). KBFC18 calculated a combined $Q$ parameter following $Q = f_{g,Q}Q_g$ (see their equation 8). We note that this couples the total $Q$ to the gas component, which we in the next section show not to be universally true, as the stellar component plays a crucial part in controlling the disc's gravitational stability.

In the KBFC18 models, gas is kept in vertical pressure and energy balance by the turbulent energy and momentum injected by gravitational instability and stellar feedback, in the form of gas transport through the disc and supernovae explosions, respectively. The gas transport equations are based on the steady state disc solution by Krumholz & Burkert (2010) assuming the disc regulates itself into marginal gravitational stability.

The authors derive relations for a number of interesting cases. Their fiducial model accounts for star formation, feedback, and gas transport (labelled 'Transport + FB'), and relates the star formation rate to the gas velocity dispersion as

$$\mathrm{SFR} = \frac{1}{2+\beta} \frac{\varphi_a f_{sf}}{\pi G Q} f_{g,Q} v_c^2 \sigma_g$$

$$\times \max\left[ \sqrt{\frac{2(1+\beta)}{3 f_{g,P}}} \varphi_{mp} \frac{8\epsilon_{ff} f_{g,Q}}{Q}, \frac{t_{orb}}{t_{sf,max}} \right]. \qquad (3)$$

This equation involves a number of free parameters that need to be assumed or calculated. We adopt the scaling factor for turbulent dissipation rate $\eta = 1.5$ and the average momentum injected by stellar feedback per unit mass $\langle p_*/m_* \rangle = 3000\,\mathrm{km\,s^{-1}}$. For all of our galaxies, we assume a rotation index $\beta = 0$, orbital period $t_{orb} = 200\,\mathrm{Myr}$, and rotation curve velocity $v_c = 230\,\mathrm{km\,s^{-1}}$. The other model parameters are described for each simulation in Table 2 along with the recommended values KBFC18 apply for these types of galaxies; local spirals and high-redshift galaxies.

The second case we consider is that of no stellar feedback (i.e. only transport, referred to as 'No-Feedback'). This is obtained by fixing $Q$ in equation (3) to a value $Q_{min}$ (=1) in order for the disc to remain in a marginally stable state.

Finally, a feedback-only model, referred to as 'No Transport, Fixed Q', is derived by considering star formation to be the only contributing factor to the system's turbulence and has the form

$$\mathrm{SFR} = \frac{4\eta \sqrt{\varphi_{mp} \varphi_{nt}^3 \varphi_a \varphi_Q}}{G Q^2 \langle p_*/m_* \rangle} \frac{f_{g,Q}^2}{f_{g,P}} v_c^2 \sigma_g^2. \qquad (4)$$

We exploit the models as intended by measuring most of the parameters in the above equations directly from the simulations.[5] Specifically, we calculate $f_{g,Q}$ (and set $f_{g,P} = f_{g,Q}$), $\varphi_{nt}$, $\varphi_Q$, and $Q = f_{g,Q}Q_g$, using the definitions in KBFC18. As prescribed by the authors, a velocity dispersion floor of $10\,\mathrm{km\,s^{-1}}$ is added to the 'Transport + FB' and 'No Transport, Fixed Q' models, representing the thermal broadening and turbulence contributed by feedback, which is missing in 'No-Feedback'. Ideally, analytic models should be able to self-sufficiently explain this plateau in order to understand the SFR–$\sigma_g$ relation, since the low-SFR regime is represented by a huge amount of galaxies. Furthermore, we have previously demonstrated (see Fig. 3) that feedback is not required to produce

---

[5]Even when adopting the values suggested by KBFC18 for low- and high-$z$ spiral galaxies (see Table 2), our conclusions remain unchanged.

**Table 2.** The parameters used in the analytical models by KBFC18, shown in equation (3) and (4). The recommended values presented here for `fg10` are given in KBFC18 as 'local spirals' and `fg50` as 'high-$z$'.

| Parameter | Recommended value | | Description |
|---|---|---|---|
| | `fg10` | `fg50` | |
| $f_{g,Q}$ | 0.5 | 0.7 | Fractional contribution of gas to $Q$ |
| $f_{g,P}$ | 0.5 | 0.7 | Fractional contribution of gas self-gravity to mid-plane pressure |
| $f_{sf}$ | 0.5 | 1.0 | Fractional of ISM in star-forming molecular phase |
| $\varphi_a$ | 1 | 3 | Offset between resolved and unresolved star formation law normalizations |
| $\varphi_Q$ | 2 | 2 | One plus ratio of gas to stellar $Q$ |
| $\varphi_{nt}$ | 1 | 1 | Fraction of velocity dispersion that is non-thermal |
| $\varphi_{mp}$ | 1.4 | 1.4 | Ratio of total pressure to turbulent pressure at mid-plane |
| $\epsilon_{ff}$ | 0.015 | 0.015 | Star formation efficiency per free-fall time |
| $t_{sf,max}$ (Gyr) | 2 | 2 | Maximum star formation time-scale |

this plateau in the SFR–$\sigma_g$ relation, which indicates that this can be driven purely by gravitational instabilities.

In Fig. 9, we directly compare $\sigma_g$ obtained from all four simulations and the three analytical models. As before, we show the results from local patches as well as global averages with the models (see Section 3.3). The dashed line indicates a one-to-one match ($\sigma_{g,sim} = \sigma_{model}$). For `fg10_FB`, all analytical models fall within the globally averaged $\sigma_g$ from the simulations.[6] While this agreement in principle is encouraging, it limits the ability to disentangle the physics of turbulence driving (provided that the simulation results are robust). All models predict higher than measured $\sigma_g$ in `fg10_noFB`, by as much as a factor of 4 in the most relevant model for comparison, 'No-Feedback'.

In the $f_g = 50$ per cent simulations, the 'No-Feedback' analytical model closely matches the globally averaged $\sigma_g$. This is in line with the conclusions made by KBFC18 that gravity is the main source of turbulence in these systems (see also Yu et al. 2019). It is noteworthy that the 'Transport + FB' model predicts values as high as $\sigma_g > 100\,\mathrm{km\,s^{-1}}$, in contrast with $\sigma_{g,sim} \sim 40$–$50\,\mathrm{km\,s^{-1}}$ measured in the simulations. As discussed above (Section 4.2.3), we argue that such high values can only be reached in tenuous gas traced by recombination lines. Related to this, less variation in $\sigma_g$ is present, for individual patches, in the simulations compared to what is predicted by the analytical models, i.e. different functional forms of the SFR–$\sigma_g$ relation are predicted. As a reminder, the average scaling of the observational data is $\sigma_g \propto \mathrm{SFR}^{0.1}$ at low SFRs and $\sigma_g \propto \mathrm{SFR}^{0.4}$ at SFR $\gtrsim 2\,\mathrm{M_\odot\,yr^{-1}}$ (see Fig. 1). This is shallower than the linear relation predicted by the models including transport $\sigma_g \propto \mathrm{SFR}$, but similar to the 'No-Transport' models with $\sigma_g \propto \mathrm{SFR}^{0.5}$.

To summarize, we find that our global averages fall within what is predicted by several of the models, but this makes it difficult to resolve what physical process is driving the SFR–$\sigma_g$ relation. The SFR–$\sigma_g$ scaling is noticeably different between model and simulation, which results in models over- and underpredicting in certain patches. We note that while the above disagreements could be interpreted as a problem of the analytical models (e.g. Bacchini et al. 2020, included disc flaring in their feedback models, which resulted in a longer dissipation time of feedback turbulence and a better match to observations), they can also signal a problem of the simulation (e.g. missing feedback physics). Finally, it is encouraging that both simulations and analytical models point to the dominating role of gravitational instabilities in driving ISM turbulence on large

scales (see also Agertz et al. 2009), but care needs to be taken when interpreting turbulence properties obtained from different gas phases.

## 5.2 Predicting $\sigma_g$ from disc stability arguments

In previous sections, we have found that the level of ISM turbulence present in our simulations is insensitive to the presence of stellar feedback, implying that gravitational instabilities is the main driver, at least on large (kpc) scales. This motivates a detailed stability analysis of the simulated galaxies.

To account for the different contributions of stars and gas on the net stability regime of a galactic disc, we adopt the multicomponent parameter $Q_{RF}$ introduced by Romeo & Falstad (2013). The general case for any number of components is defined as

$$\frac{1}{Q_{RF}} = \sum_i \left( \frac{W_i}{T_i Q_i} \right). \tag{5}$$

The term $T_i$ quantifies the stabilization effect of each component due to the thickness of the disc and reads

$$T_i = \begin{cases} 1 + 0.6 \left( \frac{\sigma_z}{\sigma_R} \right)_i^2 & \text{for } \left( \frac{\sigma_z}{\sigma_R} \right)_i \leq 0.5, \\ 0.8 + 0.7 \left( \frac{\sigma_z}{\sigma_R} \right)_i & \text{for } \left( \frac{\sigma_z}{\sigma_R} \right)_i > 0.5. \end{cases} \tag{6}$$

Finally, the term $W_i$ is used to attribute different weights to the components:

$$W_i = \frac{2\sigma_m \sigma_i}{\sigma_m^2 + \sigma_i^2}, \tag{7}$$

here $m$ denotes the least stable component,

$$T_m Q_m = \min_i \{ T_i Q_i \}. \tag{8}$$

This relation is important for differentiating between star- and gas-driven turbulence regimes, which we elaborate on in Appendix E and show that stars are the main driver in our galaxies when $f_g \lesssim 45$ per cent.

The stability of galaxies can be evaluated from the $Q$ stability parameters (see equations 2 and 5), which are shown for our simulations in Fig. 10, as a function of the distance from the galactic centre. We present $Q$ for stars, gas and a combination of these into a multicomponent $Q_{RF}$ (see Section 5.2). Note that $Q_g$ is for the total gas and that it is the cold and dense gas that contribute most to its instability; thus, this analysis is not comparable with the more turbulent warm and ionized gas phase.

Fig. 10 shows that the `fg10` discs are marginally stable, with $Q_{RF} \sim Q_\star \sim 1.5$–3 while `fg50` galaxies are slightly more stable with

---

[6]By adjusting the contribution from thermal broadening, an even closer match can in principle be achieved.
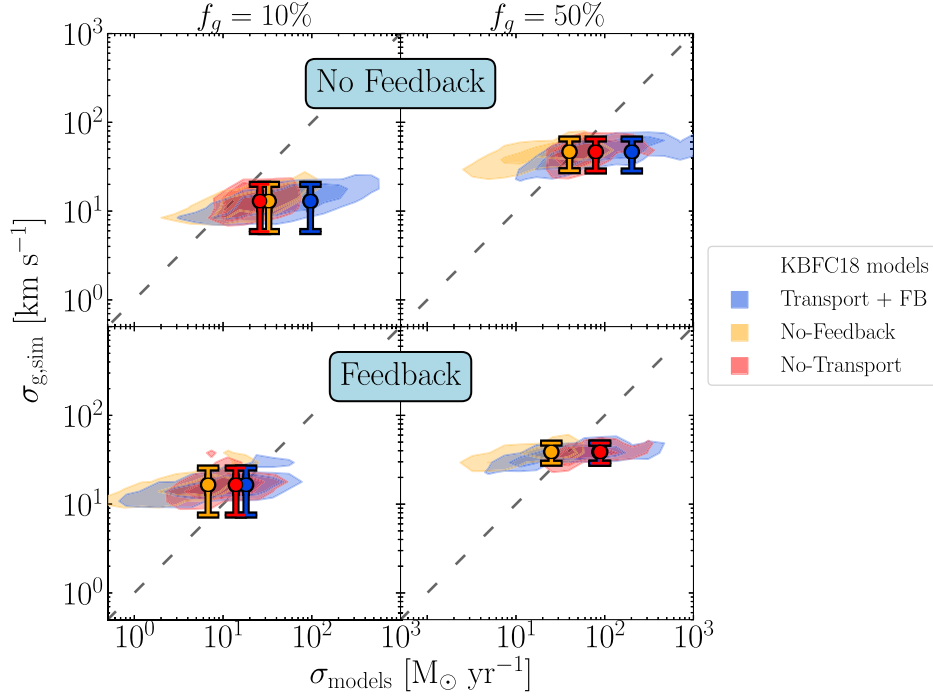
**Figure 9.** A direct comparison between the velocity dispersion from our simulations and the analytic models in KBFC18. The contours show the results from patches and the markers with error bars are the global averages (see Section 3.3). Left-hand panels are the lower gas fraction galaxy and right-hand show the higher gas fraction galaxy. The upper panels have been run without feedback while the lower panels are with feedback present. The dashed line shows $\sigma_{\rm g,sim} = \sigma_{\rm models}$.
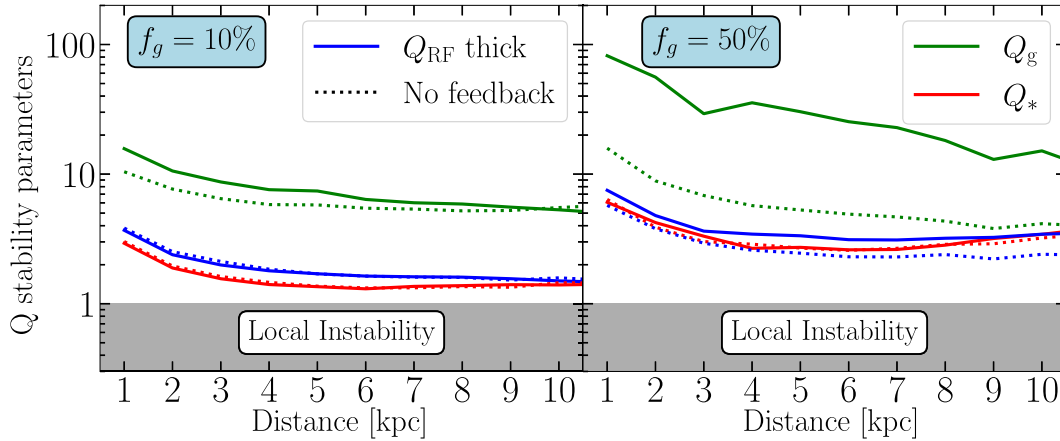


**Figure 10.** Different $Q$ stability parameters plotted against the radial distance from the centre, including all simulation runs; `fg10` on the left and `fg50` on the right. The dotted lines are the runs without any feedback. The $Q$-values shown are for the gas, stars, and the multicomponent $Q_{\rm RF}$, explained in Section 5.2. The values presented here were evaluated at the kpc-scale. The stars are seen to drive the instability and $Q_{\rm RF}$ shows that the lower gas fraction is quasi-stable while the higher gas fraction galaxy is marginally stable, independent of feedback heating.

$Q_{\rm RF} \sim Q_\star \sim 2$–4, with little dependence on feedback. The gaseous component is much higher, with $Q_{\rm g} \sim 6$–7, for `fg10` and $Q_{\rm g} \sim 10$–100 for `fg50_FB`. However, as the stars are driving the instability in all of our galaxies, the high $Q_{\rm g}$ does not affect the overall stability. We find that feedback does not significantly alter the overall stability of the disc on the scales we probe it ($\sim 1$ kpc; Renaud et al. 2021 show that discs follow the Toomre regime of instabilities at scales $\gtrsim$ a few 100 pc). This indicates that turbulence at these scales might be driven by gravitational instability.

As shown above, we find that the discs are in a marginally unstable state ($Q_{\rm RF} \sim 1.5$–4) in all simulations. As such, the stability parameter can serve as a predictor (within a factor of 2) for the gas velocity

dispersion. Re-writing the $Q_{\rm RF}$ equation to solve for the gas velocity dispersion

$$\sigma_{\rm RF} = \sigma_\star \sqrt{2\, \frac{\Sigma_{\rm g}}{\Sigma_\star} \frac{T_\star}{T_{\rm g}} \left(T_\star Q_\star / Q_{\rm RF} - 1\right)^{-1} - 1}, \tag{9}$$

where we have assumed stars drive the instability. This predictive equation is easily applicable to data of disc galaxies where the velocity dispersions and surface densities of the gas and stars are known. In particular, for our analysis we measured $\Sigma_{\rm g}$, $\Sigma_\star$, $\sigma_{\rm g}$, $\sigma_\star$, $Q_\star$ from the simulations and then assumed $T_\star \approx 1.2$, $T_{\rm g} \approx 1.5$, and $Q_{\rm RF} \approx 2.2$ (as measured for local disc galaxies Leroy et al. 2008; Romeo & Falstad 2013; Romeo & Mogotsi 2017).
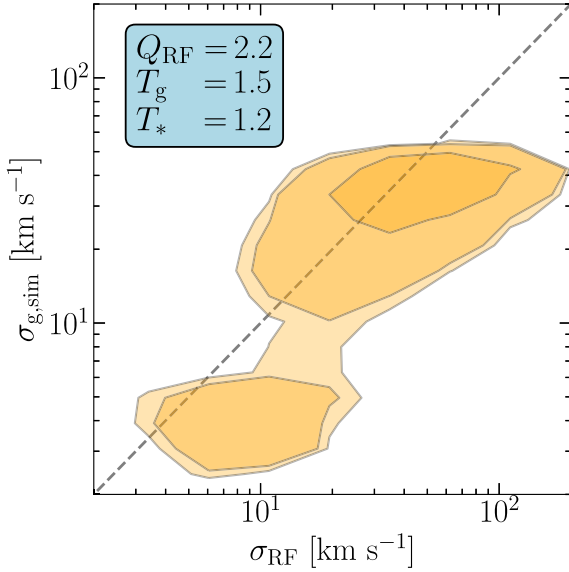
**Figure 11.** A direct comparison between the $\sigma_g$ calculated from simulations and the $\sigma_g$ predicted by a combined $Q$ parameter recipe from Romeo & Falstad (2013), see equation (9). We find an encouraging match between $\sigma_{RF}$ and the simulation data. The $\sigma_{RF}$ values are seen to cluster around 50 and $10\,km\,s^{-1}$. The lower values arise due to the significantly different stability conditions occurring in the outer region of the galaxy, where other physical processes might balance against gravitational collapse.

In Fig. 11, we compare this analytic equation with our simulated $\sigma_g$ for a marginally unstable disc. This figure demonstrates that the $Q_{RF}$ approximation can predict the level of turbulence in disc galaxies. Furthermore, we discern two regions for the contoured data; below and above $\sigma_{g,sim} \sim 6$–$10\,km\,s^{-1}$. The lower $\sigma_g$ mainly represent the outskirts of the galaxy, $\gtrsim 10\,kpc$. This might indicate that different processes might be driving the turbulence in the outer and inner parts of the galaxy.

## 6 CONCLUSIONS

In this paper, we present hydrodynamical simulations of isolated disc galaxies in order to evaluate how observational parameters shape the SFR–$\sigma_g$ relation. The available data from observations is highly heterogeneous and the various effects need to be carefully considered in order to analyse the underlying driver of this relation. Then, we compare the velocity dispersion predicted by theoretical models with our simulations. Our findings can be summarized as follows:

(i) Our simulations reproduce key features in the observed SFR–$\sigma_g$ relation: the plateau at $\sigma_g \sim 10\,km\,s^{-1}$ for SFR$\lesssim 2\,M_\odot\,yr^{-1}$ and the exponential growth towards larger $\sigma_g$ for SFR$\gtrsim 2\,M_\odot\,yr^{-1}$. This result is independent of whether stellar feedback is included or not, and is hence an outcome of how galactic discs regulate their gravitational stability [see point (v) below].

(ii) Our most turbulent galaxies, fg50, reach at most $\sigma_g \sim 50\,km\,s^{-1}$ at SFR $\sim 10$–$50\,M_\odot\,yr^{-1}$, while the velocity dispersions of high-redshift galaxies have been observed to reach $\sigma_g \sim 100\,km\,s^{-1}$. We demonstrated that $\sigma_g > 50\,km\,s^{-1}$ can partially be explained by beam smearing. If unaccounted for, or accounted for insufficiently, even galaxy inclinations as low as $\theta = 30°$ can increase the observed velocity dispersions by factors of several. High-redshift galaxies are poorly resolved, and tend to have complex morphologies due to fragmentation and merging. It is therefore possible that beam

smearing leads to overestimated levels of gas turbulence in those galaxies.

(iii) While stellar feedback does not change the SFR–$\sigma_g$ relation for the total gas content, it affects the level of turbulence in the warm ionized gas phase, here traced by the H$\alpha$ transition. In this gas phase, feedback significantly increases $\sigma_g \sim 50\,km\,s^{-1}$ to $\sigma_g \sim 100\,km\,s^{-1}$. As stated above, this is in good agreement with what is found in high-redshift galaxies, especially given that those observations have predominantly surveyed them in H$\alpha$. However, it further highlights that different gas tracers do not trace the same gas kinematic and, thus, that the available SFR–$\sigma_g$ data do not follow one universal relation. Furthermore, we formulated a simple equation of the turbulent energy budget (see Appendix C) and find that only 10 per cent of the total turbulent energy needs to be in the warm ionized gas phase (traced by H$\alpha$) in order to reproduce the high $\sigma_{H\alpha}$ reported.

(iv) Analytic models for the SFR–$\sigma_g$ relation for gravitational instability and stellar feedback, taken from literature, can in principle reproduce the observed high velocity dispersion in rapidly star forming high-redshift galaxies. However, the parameters adopted in these models can be uncertain, and the functional form of the predicted SFR–$\sigma_g$ relation does not match that of the simulations.

(v) The simulated galaxies are, when both stars and gas are accounted for, naturally drawn towards a state of marginal stability, with a $Q$ stability level of $Q \sim 1$–$3$, *independent* of the source of the heating (galactic dynamics or stellar feedback). As mentioned above, this appears to be a fundamental property of galactic discs. As such, a multicomponent $Q$ parameter is a valuable analysis tool for predicting levels of gas turbulence in disc galaxies. We exploited the combined $Q_{RF}$ (Romeo & Falstad 2013) to solve for $\sigma_g$ and found that even if assuming certain parameter values, this analytic relation can reproduce the gas turbulence within our simulations. Thus, it could possibly be applied to observational data to predict the turbulence of isolated disc galaxies.

In this work, we have studied isolated disc galaxies, which means that cosmological effects, such as accretion and mergers, are not present. These effects would mix the ISM and possibly give rise to more turbulent motion. Indirectly, accretion would help sustain the turbulence in the galaxy over a longer period of time by continuously supplying gas for consistent star formation (and stellar feedback). Furthermore, a number of feedback process present in galaxies are not accounted for (e.g. feedback from active galactic nuclei, cosmic rays). Despite neglecting these factors, we are able to match the observed SFR–$\sigma_g$ relation, which implies that disc galaxies do not necessarily require these effects to remain in a marginally stable state or sustain their high levels of turbulence.

For this project, we have made use of NUMPY (Harris et al. 2020) and MATPLOTLIB for PYTHON (Hunter 2007). Visualization of the simulation volume and handling the data was done using the YT project (Turk et al. 2011).

## DATA AVAILABILITY

The data underlying this article will be shared on reasonable request to the corresponding author.

## REFERENCES

Agertz O., Lake G., Teyssier R., Moore B., Mayer L., Romeo A. B., 2009, MNRAS, 392, 294

Agertz O., Kravtsov A. V., Leitner S. N., Gnedin N. Y., 2013, ApJ, 770, 25

Agertz O., Romeo A. B., Grisdale K., 2015, MNRAS, 449, 2156

Alcorn L. Y. et al., 2018, ApJ, 858, 47

Armillotta L., Krumholz M. R., Fujimoto Y., 2018, MNRAS, 481, 5000

Bacchini C., Fraternali F., Iorio G., Pezzulli G., Marasco A., Nipoti C., 2020, A&A, 641, A70

Ballesteros-Paredes J., Klessen R. S., Mac Low M. M., Vazquez-Semadeni E., 2007, in Reipurth B., Jewitt D., Keil K., eds, Protostars and Planets V. p. 63

Caldú-Primo A., Schruba A., Walter F., Leroy A., Sandstrom K., de Blok W. J. G., Ianjamasimanana R., Mogotsi K. M., 2013, AJ, 146, 150

Callaway J., Unnikrishnan K., Oza D. H., 1987, Phys. Rev. A, 36, 2576

Chabrier G., 2003, PASP, 115, 763

Cresci G. et al., 2009, ApJ, 697, 115

Davies R. et al., 2011, ApJ, 741, 69

Dekel A. et al., 2009a, Nature, 457, 451

Dekel A., Sari R., Ceverino D., 2009b, ApJ, 703, 785

Di Teodoro E. M., Fraternali F., 2015, MNRAS, 451, 3021

Di Teodoro E. M., Fraternali F., Miller S. H., 2016, A&A, 594, A77

Dib S., Bell E., Burkert A., 2006, ApJ, 638, 797

Dijkstra M., 2017, preprint (arXiv:1704.03416)

Elmegreen B. G., Burkert A., 2010, ApJ, 712, 294

Elmegreen B. G., Scalo J., 2004, Annu. Rev. Astron. Astrophys., 42, 211

Elmegreen D. M., Elmegreen B. G., Ravindranath S., Coe D. A., 2007, ApJ, 658, 763

Elmegreen B. G., Elmegreen D. M., Fernandez M. X., Lemonias J. J., 2009, ApJ, 692, 12

Epinat B., Amram P., Marcelin M., 2008, MNRAS, 390, 466

Epinat B. et al., 2009, A&A, 504, 789

Faucher-Giguère C.-A., Quataert E., Hopkins P. F., 2013, MNRAS, 433, 1970

Federrath C., 2018, Phys. Today, 71, 38

Förster Schreiber N. M. et al., 2006, ApJ, 645, 1062

Genel S., Dekel A., Cacciato M., 2012, MNRAS, 425, 788

Genzel R. et al., 2011, ApJ, 733, 101

Ginzburg O., Dekel A., Mandelker N., Krumholz M. R., 2022, preprint (arXiv:2202.12331)

Girard M. et al., 2021, ApJ, 909, 12

Glazebrook K., 2013, Publ. Astron. Soc. Aust., 30, e056

Goldreich P., Lynden-Bell D., 1965, MNRAS, 130, 97

Grisdale K., Agertz O., Romeo A. B., Renaud F., Read J. I., 2017, MNRAS, 466, 1093

Grisdale K., Agertz O., Renaud F., Romeo A. B., 2018, MNRAS, 486, 5842

Grisdale K., Agertz O., Renaud F., Romeo A. B., Devriendt J., Slyz A., 2019, MNRAS, 486, 5482

Guillet T., Teyssier R., 2011, J. Comput. Phys., 230, 4756

Hafen Z. et al., 2022, preprint (arXiv:2201.07235)

Harris C. R. et al., 2020, Nature, 585, 357

Hayward C. C., Hopkins P. F., 2017, MNRAS, 465, 1682

Hernquist L., 1990, ApJ, 356, 359

Hernquist L., 1993, ApJS, 86, 389

Heyer M., Krawczyk C., Duval J., Jackson J. M., 2009, ApJ, 699, 1092

Hui L., Gnedin N. Y., 1997, MNRAS, 292, 27

Hung C.-L. et al., 2019, MNRAS, 482, 5125

Hunter J. D., 2007, Comput. Sci. Eng., 9, 90

Ianjamasimanana R., de Blok W. J. G., Walter F., Heald G. H., 2012, AJ, 144, 96

Józsa G. I. G., Kenn F., Klein U., Oosterloo T. A., 2007, A&A, 468, 731

Kamphuis P., Józsa G. I. G., Oh S.. H., Spekkens K., Urbancic N., Serra P., Koribalski B. S., Dettmar R. J., 2015, MNRAS, 452, 3139

Kim C.-G., Ostriker E. C., 2015, ApJ, 802, 99

Kim J.-h. et al., 2014, ApJS, 210, 14

Kim J.-h. et al., 2016, ApJ, 833, 202

Klessen R. S., Hennebelle P., 2010, A&A, 520, A17

Kohandel M., Pallottini A., Ferrara A., Carniani S., Gallerani S., Vallini L., Zanella A., Behrens C., 2020, MNRAS, 499, 1250

Kritsuk A. G., Norman M. L., Padoan P., Wagner R., 2007, ApJ, 665, 416

Krumholz M., Burkert A., 2010, ApJ, 724, 895

Krumholz M. R., Burkhart B., 2016, MNRAS, 458, 1671

Krumholz M. R., McKee C. F., Tumlinson J., 2009, ApJ, 693, 216

Krumholz M. R., Burkhart B., Forbes J. C., Crocker R. M., 2018, MNRAS, 477, 2716  (KBFC18)

Larson R. B., 1981, MNRAS, 194, 809

Law D. R., Steidel C. C., Erb D. K., Larkin J. E., Pettini M., Shapley A. E., Wright S. A., 2009, ApJ, 697, 2057

Lehnert M. D., Nesvadba N. P. H., Le Tiran L., Di Matteo P., van Driel W., Douglas L. S., Chemin L., Bournaud F., 2009, ApJ, 699, 1660

Lehnert M. D., Le Tiran L., Nesvadba N. P. H., van Driel W., Boulanger F., Di Matteo P., 2013, A&A, 555, A72

Lemoine-Busserolle M., Bunker A., Lamareille F., Kissler-Patig M., 2010, MNRAS, 401, 1657

Leroy A. K., Walter F., Brinks E., Bigiel F., de Blok W. J. G., Madore B., Thornley M. D., 2008, AJ, 136, 2782

Levy R. C. et al., 2018, ApJ, 860, 92

Mac Low M.-M., Klessen R. S., 2004, Rev. Mod. Phys., 76, 125

Martizzi D., Faucher-Giguère C.-A., Quataert E., 2015, MNRAS, 450, 504

McKee C. F., Ostriker E. C., 2007, ARA&A, 45, 565

Moiseev A. V., Tikhonov A. V., Klypin A., 2015, MNRAS, 449, 3568

Molina J., Ibar E., Smail I., Swinbank A. M., Villard E., Escala A., Sobral D., Hughes T. M., 2019, MNRAS, 487, 4856

Molina J. et al., 2020, A&A, 643, A78

Navarro J. F., Frenk C. S., White S. D. M., 1996, ApJ, 462, 563

Nguyen-Luong Q. et al., 2016, ApJ, 833, 23

Nusser A., Silk J., 2022, MNRAS, 509, 2979

Orr M. E., Hayward C. C., Hopkins P. F., 2019, MNRAS, 486, 4724

Orr M. E. et al., 2020, MNRAS, 496, 1620

Padoan P. et al., 2014, in Beuther H., Klessen R. S., Dullemond C. P., Henning T., eds, Protostars and Planets VI. UAPress, Arizona, p. 77

Patrício V. et al., 2018, MNRAS, 477, 18

Peng C. Y., Ho L. C., Impey C. D., Rix H.-W., 2002, AJ, 124, 266

Renaud F., Kraljic K., Bournaud F., 2012, ApJ, 760, L16

Renaud F., Bournaud F., Kraljic K., Duc P. A., 2014, MNRAS, 442, L33

Renaud F., Romeo A. B., Agertz O., 2021, MNRAS, 508, 352

Rhodin N. H. P., Agertz O., Christensen L., Renaud F., Fynbo J. P. U., 2019, MNRAS, 488, 3634

Rizzo F., Vegetti S., Fraternali F., Stacey H. R., Powell D., 2021, MNRAS, 507, 3952

Romeo A. B., Falstad N., 2013, MNRAS, 433, 1389

Romeo A. B., Fathi K., 2015, MNRAS, 451, 3107

Romeo A. B., Fathi K., 2016, MNRAS, 460, 2360

Romeo A. B., Mogotsi K. M., 2017, MNRAS, 469, 286

Rosen A., Bregman J. N., 1995, ApJ, 440, 634

Safronov V. S., 1960, Ann. Astrophys., 23, 979

Springel V., 2000, MNRAS, 312, 859

Stilp A. M., Dalcanton J. J., Skillman E., Warren S. R., Ott J., Koribalski B., 2013, ApJ, 773, 88

Storey P. J., Hummer D. G., 1995, MNRAS, 272, 41

Sutherland R. S., Dopita M. A., 1993, ApJS, 88, 253

Tamburro D., Rix H.-W., Leroy A. K., Mac Low M.-M., Walter F., Kennicutt R. C., Brinks E., de Blok W. J. G., 2009, AJ, 137, 4424

Teyssier R., 2002, A&A, 385, 337

Toomre A., 1964, ApJ, 139, 1217

Turk M. J., Smith B. D., Oishi J. S., Skory S., Skillman S. W., Abel T., Norman M. L., 2011, ApJS, 192, 9
van Albada T. S., Bahcall J. N., Begeman K., Sancisi R., 1985, ApJ, 295, 305
van Donkelaar F., Agertz O., Renaud F., 2022, MNRAS, 512, 3806
Varidel M., Pracy M., Croom S., Owers M. S., Sadler E., 2016, Publ. Astron. Soc. Aust., 33, e006
Varidel M. R. et al., 2020, MNRAS, 495, 2265
Veilleux S., Cecil G., Bland-Hawthorn J., 2005, ARA&A, 43, 769
Walter F., Brinks E., de Blok W. J. G., Bigiel F., Kennicutt Robert C. J., Thornley M. D., Leroy A., 2008, AJ, 136, 2563
Wisnioski E. et al., 2011, MNRAS, 417, 2601
Yang C.-C., Krumholz M., 2012, ApJ, 758, 48
Yu X. et al., 2019, MNRAS, 486, 4463
Yu X., Bian F., Krumholz M. R., Shi Y., Li S., Chen J., 2021, MNRAS, 505, 5075
Zanella A. et al., 2019, MNRAS, 489, 2792

Zhou L. et al., 2017, MNRAS, 470, 4573
Übler H. et al., 2018, ApJ, 854, L24
Übler H. et al., 2019, ApJ, 880, 48

## APPENDIX A: OBSERVATIONAL DATA

This appendix contains a table, Table A1, with a compilation of literature references, from which we collected the values of $\sigma_g$ and the SFR. Each reference is associated with a marker, which are used in figures throughout this article. Furthermore, we have summarized some of the more useful properties of these observations in the table: the survey/telescope employed, the tracer used to calculate $\sigma_g$, the spatial area probed, the approximate redshift (local or high redshift), and whether the observations were corrected for the inclination of the galaxy.

**Table A1.** The complete literature library of the observational data of SFR and $\sigma_g$. The data compiled by us are from the SFR derived by Walter et al. (2008) and the (instrument free) $\sigma_g$ is from Tamburro et al. (2009). This table relates each reference to a marker, which are used throughout this paper when plotting quantities from that reference. Note that the observational spatial resolution and redshifts are approximate and the typical medians of the respective sample. Galaxies noted with a redshift 'local' were observed at redshifts much smaller than 1, but the precise redshift is commonly not specified. The data of this table are very heterogeneous, i.e. the observations are of different types of disc galaxies (e.g. normal, dwarf, merged galaxies) with different crucial properties (e.g. mass, morphology). A more thorough explanation of the data and its heterogeneity can be found in Section 2.

| Reference name | Survey/instrument | Tracer | Spatial resolution | Redshift | Beam corrected | Mark |
|---|---|---|---|---|---|---|
| Alcorn et al. (2018) | ZFIRE | H$\alpha$ | ~4 kpc | 2.2 | Yes | ○ |
| Cresci et al. (2009) | SINFONI/ SINS | H$\alpha$ | ~3 kpc | 2 | Yes | △ |
| Di Teodoro et al. (2016) | KMOS | H$\alpha$ | ~5 kpc | 1 | Yes | ▷ |
| Compiled by us (see table description) | THINGS | H$I$ | 0.1–0.5 kpc | Local | Yes | ○ |
| Epinat et al. (2009) | SINFONI | H$\alpha$ | ~5 kpc | 1.2–1.6 | Yes | ◁ |
| Genzel et al. (2011) | SINS | H$\alpha$ | ~2 kpc | 2.3 | Yes | ◇ |
| Girard et al. (2021) (ionized gas) | SINS | H$\alpha$ | ~1 kpc | Local (& 1–2) | Yes | ▽ |
| Girard et al. (2021) (molecular gas) | SINS | CO | 2 kpc | Local (& 1–2) | Yes | ● |
| Ianjamasimanana et al. (2012) | THINGS | H$I$ | sub-kpc | Local | Yes | ◆ |
| Compiled by Krumholz et al. (2018) | SIMBAD | CO/HCN | sub-kpc | Local | No | ◆ |
| Law et al. (2009) | Keck/ OSIRIS | H$\alpha$, [O III] | 1.2 kpc | ~2.3 | No | ☆ |
| Lehnert et al. (2013) | SINFONI | H$\alpha$, [N II] | ~5 kpc | 1−3 | No | △ |
| Lemoine-Busserolle et al. (2010) | VLT/ SINFONI | UV (H$\beta$ / [O III]) | ~4 kpc | 3.3 | Yes | ● |
| Levy et al. (2018) | EDGE-CALIFA | CO | sub-kpc | Local | Yes | △ |
| Moiseev et al. (2015) | 6-m tele. SAO RAS | H$\alpha$ | sub-kpc | Local | No | ■ |
| Nguyen-Luong et al. (2016) | CfA 1.2 m telescopes | CO | sub-kpc | Milky Way | No | ◆ |
| Patrício et al. (2018) | MUSE | [O II] | sub-kpc | 0.6−1.5 | Yes | ✖ |
| Stilp et al. (2013) | THINGS and VLA-ANGST | H$I$ | 0.2 kpc | Local | Yes | ◆ |
| Varidel et al. (2016) | SDSS | H$\alpha$ | ~1 kpc | Local | Yes | ◇ |
| Wisnioski et al. (2011) | WiggleZ | UV, [O II] | 0.8 kpc | 1.3 | No | ◇ |
| Yu et al. (2019) | MaNGA | H$\alpha$ | 1 kpc | 0.01–0.15 | Yes | ⬡ |
| Zhou et al. (2017) | SAMI | H$\alpha$ | 2.5 kpc | 0.05 | Yes | ⬡ |
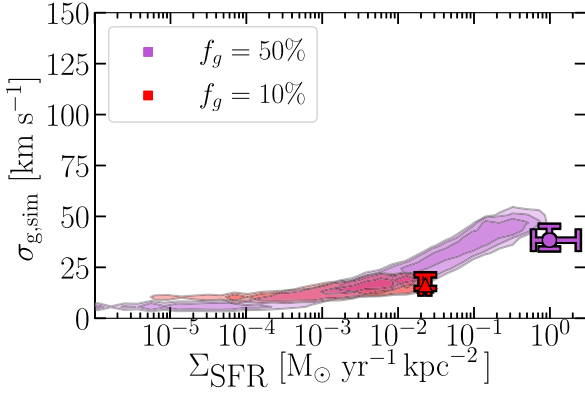
**Figure B1.** The $\sigma_{\mathrm{g}}$–$\Sigma_{\mathrm{SFR}}$ relation for the two feedback simulations, using data with patch sizes $\leq 8\,\mathrm{kpc}$ and no inclination. The contours show the patch-based data and the global values are represented by markers with error bars, as described in Section 3.3. There is a clear correlation between the turbulence and star formation density, which exhibits similar properties as the SFR–$\sigma_{\mathrm{g}}$ relation.

## APPENDIX B: STAR FORMATION DENSITY

In order to get a view of how star formation affects turbulence regardless of patch size, we plot $\sigma_{\mathrm{g}}$ against $\Sigma_{\mathrm{SFR}}$ in Fig. B1. This relation is in agreement with Orr et al. (2020) and is essentially the same as Fig. 3, but takes into account the patch size of each observed point and is, by comparison, less dispersed. As discussed in Section 4.2.1, two patches of different sizes with identical SFR will exhibit different densities of star formation. Thus, the smaller patch will have a higher column star formation density, which leads to more intense turbulence since star formation events increase $\sigma_{\mathrm{g}}$.

## APPENDIX C: ANALYTIC RECIPE FOR H$\alpha$ EMISSIVITY

We evaluated the warm ionized phase using emissivity equations from theoretical work, assuming the phase is well traced by the H$\alpha$ transition. We only consider the H$\alpha$ emissivity contribution from the 3p $\rightarrow$ 2s transition in hydrogen, since the contribution to the emission intensity of other transitions is comparably small. Emissivity has the general shape

$$\epsilon_{\mathrm{H}\alpha} = n_e n_H h \nu q, \tag{C1}$$

where $\nu$ is the light frequency, $h$ is the Planck constant, and $q$ is the emission rate. From RAMSES, we can extract the electron density $n_e$ and hydrogen density $n_H$ of the gas. The energy of the H$\alpha$ emission is $h\nu = 3.026 \times 10^{-12}\,\mathrm{erg}$. For this analysis, we consider both the emissivity coming from collisional excitation and recombination. The collisional excitation rate is given by

$$q_{\mathrm{coll}}(T) = \frac{1.3 \times 10^{-6}}{T^{0.5}} \left(\frac{T}{11.2}\right)^{0.305} \times \exp\left(\frac{-h\nu}{kT}\right) \tag{C2}$$

and was determined by fitting data from Callaway, Unnikrishnan & Oza (1987). The recombination rate (following the formalism in Dijkstra 2017) is given by

$$q_{\mathrm{recom}} = \epsilon_{\mathrm{H}\alpha}^{B}(T)\alpha_{\mathrm{B}}(T), \tag{C3}$$

where

$$\epsilon_{\mathrm{H}\alpha}^{B}(T) = 8.176 \times 10^{-8} - 7.46 \times 10^{-3}\,\log_{10}(T/10^4)$$
$$+ 0.451\,01\,(T/10^4)^{-0.1013} \tag{C4}$$

is the emitted rate of H$\alpha$; the shape is fitted using observational values from Storey & Hummer (1995). Finally,

$$\alpha_{\mathrm{B}}(T) = 2.753 \times 10^{-14} \left(\frac{315\,614}{T}\right)^{1.5} \left(1 + \left(\frac{315\,614}{T}\right)^{0.407}\right)^{-2.42} \tag{C5}$$

is the probability that the cascade from hydrogen recombination, called case B recombinations, emits an H$\alpha$ photon (fit from Hui & Gnedin 1997). The two $q$ values are then added linearly to calculate the total emissivity.

## APPENDIX D: H$\alpha$ TURBULENT ENERGY INPUT

We showed in Section 4.2.3 that it is only through the warm ionized phase that we can achieve the large $\sigma_{\mathrm{g}}$ observed at high-$z$, we next quantify the required energy input in order to achieve this high turbulence in the H$\alpha$ tracer. By applying the simplistic assumption that turbulent energy in the ISM is conserved between all phases, we can derive the velocity dispersion of the ionized phase. Essentially, we assume that a fraction of the total turbulent energy is in the warm ionized phase, $F_{\mathrm{H}\alpha}$. This yields

$$\sigma_{\mathrm{H}\alpha} = \sigma_{\mathrm{g}} \sqrt{\frac{F_{\mathrm{H}\alpha}}{f_{\mathrm{m,H}\alpha}}}, \tag{D1}$$

where $f_{\mathrm{m,H}\alpha}$ is the fraction of mass detectable in H$\alpha$. Particularly, $F_{\mathrm{H}\alpha}$ is a free parameter that tells us how much energy needs to be injected into the ionized gas phase in order to reach the $\sigma_{\mathrm{H}\alpha}$ observed.

In Fig. D1, we plot this equation against the $\sigma_{\mathrm{H}\alpha}$ using data from the `fg_50FB` simulation (showing only the patch-based approach). The comparison shows a remarkable agreement in values and scaling between analytic equation and simulation. The best match is given
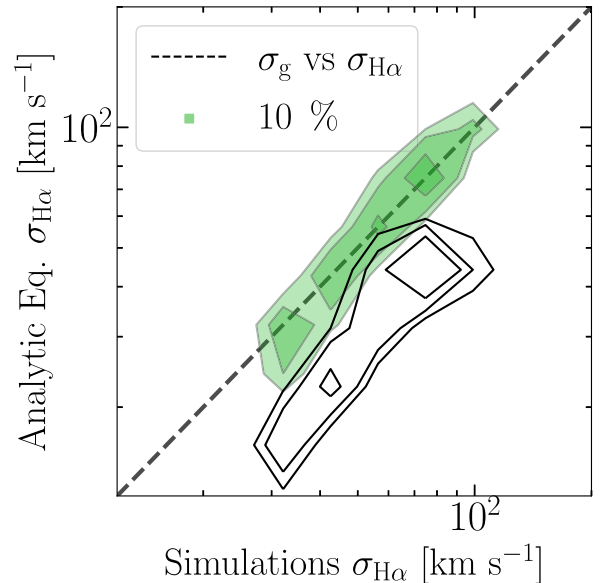


**Figure D1.** The relation between the $\sigma_{\mathrm{H}\alpha}$ from a simplistic relation, shown in equation (D1), and $\sigma_{\mathrm{H}\alpha}$ calculated from simulations. This plot uses data from `fg_50FB` and defines the H$\alpha$ phase to temperature cuts ($6 \times 10^3\,\mathrm{K} \leq T \leq 2 \times 10^4\,\mathrm{K}$), in order to calculate the gas fraction of the phase. The dotted diagonal line shows where the equation and the simulation agrees. Different factors for the energy contributed by H$\alpha$ were tried and the best agreement was found to be $F_{\mathrm{H}\alpha} \approx 10$ per cent. As a comparison, the black contours show the relation of the calculated $\sigma_{\mathrm{g}}$ (of all the gas) and $\sigma_{\mathrm{H}\alpha}$ from the simulations.

when roughly 10 per cent of the turbulent energy is in H$\alpha$, which is assumed a global factor here, but might vary in the local environment of the patch. Furthermore, a comparison of how $\sigma_g$ for the total gas scales with $\sigma_{H\alpha}$ (calculated) is plotted as a dashed region to illustrate how the calculated $\sigma_g$ is transformed. Note that in order to calculate the mass from our simulations we have here applied temperature cuts ($6 \times 10^3$ K $\leq T \leq 2 \times 10^4$ K) to evaluate the H$\alpha$ tracer (instead of the emissivity analytic equations), which was tested and found to give very similar $\sigma_g$ to our more detailed approach in Section 4.2.3.

## APPENDIX E: IS INSTABILITY DRIVEN BY GAS OR STARS?

The instability of the galactic disc is driven by its two components, gas and stars. Investigating the main driver of this instability is useful in the case that gravitational instability drives turbulent gas motion in the disc. In order to evaluate each components contribution to drive

instability, we calculated the mass fraction of gas which is marginally unstable ($Q \lesssim 2$) in the disc and plot it against the gas fraction, seen in Fig. E1. We analyse the $Q$ stability parameters for the gas, stars and the combined $Q_{RF}$ for a thick disc. The region in which gas dominates the instability is shown as a dashed line and is determined from equation (5). The dependence of the stability with gas fraction (and thus, time) is evident, as the gas mass fraction that is gravitational unstable is significantly higher in the earlier lifetime of the galaxy. Gas dominates the instability for a very limited time in the high gas fraction, ending after only a small fraction of the gas had been turned into stars. Furthermore, for the galaxies without feedback the gas dominated the disc instability far longer. This makes sense from the perspective that stellar feedback heats up the gas, while the stars remain kinematically cold (see van Donkelaar et al. 2021). Note that the decision to consider values corresponding to a marginally stable disc is motivated by Fig. 10 (see also the discussion in Section 5.1), in which it is evident that the higher gas fraction galaxy does not go far below this threshold.
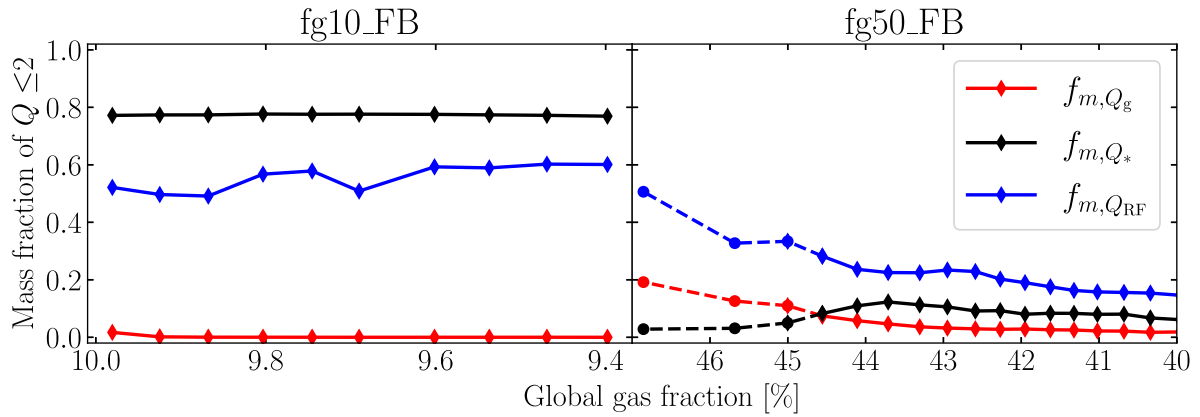


**Figure E1.** The fraction of mass in a marginally stable state disc ($Q \leq 2$) as a function of the total gas fraction of the galaxy. Dashed lines (seen for gas fractions $f_g \geq 45$ per cent) correspond to the region in which the instability is dominated by the gas. A clear transition from gas- to star-driven instability is seen to occur early in the evolution of the fg50_FB galaxy. For the most part, stars are the main drivers of instability in our galaxies.

This paper has been typeset from a TEX/LATEX file prepared by the author.